STUDY OF STRUCTURAL, MAGNETIC, AND ELECTRICAL PROPERTIES OF Mg SUBSTITUTED Ni-Cu-Cd BULK FERRITES OBTAINED FROM NANOCRYSTALLINE POWDERS.

By

Md. Shahbaz Khan

Student ID: 20MSPHY006F

A thesis submitted in partial fulfillment of the requirement for the degree of

MASTER of SCIENCE

Department of Physics

CHITTAGONG UNIVERSITY OF ENGINEERING AND TECHNOLOGY

OCTOBER 2024

Declaration of Candidate

I hereby declare that the work contained in this Thesis has not been previously submitted to meet the requirements for an award at this or any other higher education institution. To the best of my knowledge and belief, the Thesis contains no materials previously published or another person except where due reference is cited. Furthermore, the Thesis complies with the PLAGIARISM and ACADEMIC INTEGRITY regulations of CUET.

Md. Shahbaz Khan

Student ID: 20MSPHY006F

Department of Physics

Chittagong University of Engineering and Technology (CUET)

Dedication

Dedicated to my Parents

and

all the people who supported my

research work.

List of Publication

Journal Article

- Md. Shahbaz Khan, Arjumanara Bagum, M. Faishal Mahmood, Nur Mohammed and M. Belal Hossen "Effects of Mg Substitution on the Structural with Rietveld Analysis, Magnetic and Magnetocaloric Properties of Ni-Cu-Cd Bulk Ceramics" J. Magn. Magn. Mater. (2024) 603 172263, June 2024, https://doi.org/10.1016/j.jmmm.2024.172263.

Conference Participation

- M. Shahbaz Khan and M. Belal Hossen "Structural investigation and dynamic study of electric, dielectric, and modulus spectroscopy of Ni-Cu-Cd-Mg bulk ferrites obtained from nanocrystalline powder." BCSIR Congress – 2022, BCSIR Dhaka, 01-03 December 2022, Page - 94.
- M. Shahbaz Khan and M. Belal Hossen "Investigation of structure with Rietveld refinement analysis and impedance spectroscopy of Mg substitution in Ni-Cu-Cd bulk ceramic obtained from nanocrystalline ferrite." Seventh Conference of Bangladesh Crystallographic Association – 2022, BUET Dhaka, 08-09 December 2022, Page - 86.
- M. Shahbaz Khan and M. Belal Hossen "Investigation of Structure with XRD Analysis, Impedance Spectroscopy, and Optical Property Analysis of Ni-Mg-Cu-Cd Dense Ceramic Obtain from Nanocrystalline Ferrites." National Conference on Physics -2023, JU Dhaka, 09-11 March 2023, Page – 68.
- M. Shahbaz Khan and M. Belal Hossen "Structural and Impedance Spectroscopy Analysis on Rietveld Refined Mg Substituted Ni-Cu-Cd Bulk Ferrite Obtained from Nanocrystalline Ferrites." 1st National Research fair – 2023, CUET Chattogram, 28 August 2023, Page – 46.
- M. Shahbaz Khan and M. Belal Hossen "Investigation of structural, optical, magnetic and electrical properties of Mg substituted Ni-Cu-Cd bulk ferrites obtained from Sol-gel synthesized Nanocrystalline powder." 5th International Conference on Physics for Sustainable Development and Technology (ICPSDT) – 2023, CUET Chattogram, 07-08 September 2023, Page – 144.

Declaration by the Supervisor

This is to certify that Md. Shahbaz Khan, Student ID 20MSPHY006F has carried out this research work under my supervision and, he has fulfilled the relevant Academic Ordinance of Chittagong University of Engineering and Technology so that he is qualified to submit the following Thesis in the application for the degree of MASTER of SCIENCE in Physics. Furthermore, the Thesis complies with the PLAGIARISM and ACADEMIC INTEGRITY regulations of CUET.

Mohammad Belal Hossen, Ph.D.
Professor
Department of Physics
Chittagong University of Engineering and Technology (CUET)

Acknowledgment

I would like to express my heartfelt gratitude to all those who have supported me throughout the journey of completing this thesis.

First and foremost, I am deeply thankful to my thesis supervisor, Mohammad Belal Hossen, for their unwavering guidance, invaluable insights, and continuous encouragement. Their expertise and mentorship have been instrumental in shaping this work.

I am pleased to express my deep appreciation to Professor Dr. H.M.A.R. Maruf, Head of the Department of Physics, Chittagong University of Engineering and Technology (CUET) for his great interest, continuous help and valuable scientific discussions during this work.

I am also indebted to the faculty members of the CUET, whose teachings and constructive feedback have been essential to my academic development.

I extend my appreciation to my friends and family for their unwavering support and understanding during the long hours and countless sacrifices that went into this research. Their love and encouragement kept me motivated throughout.

I would like to acknowledge the participants of this study, without whom this research would not have been possible. Your willingness to share your experiences and insights has contributed significantly to the depth and quality of this thesis.

Lastly, I am grateful to the researchers and superiors whose work laid the foundation for this thesis. Their contributions have been invaluable in shaping my understanding of the subject matter.

This journey has been challenging, but it has been made more bearable thanks to the support and guidance I have received. I am profoundly grateful to everyone who has been a part of this endeavor.

Thank you

Md. Shahbaz Khan

Abstract

Bulk ceramics with optimized density are highly prioritized over ferrite nanoparticles to fabricate devices for their optimal magnetic saturation, lower coercivity, and anisotropy, enhanced resistance, etc. To achieve such bulk specimen using $Ni_{0.5-y}Mg_yCu_{0.2}Cd_{0.3}Fe_2O_4$ disc and toroid samples are sintered at 1423 K keeping the heating and cooling rate at 10 K and 5 K respectively. In this course, structural as well as theoretical Rietveld analysis, optical, and magnetic dielectric and electrical properties have been analyzed using these bulk samples. XRD has explored structural properties and after that these values have analyzed with the Rietveld refinement procedure and obtained goodness of χ^2 (1–2) value and other parameters such as lattice parameters, crystal structures, cation distribution, and maximum entropy mapping. Surface morphology and grain size have examined from the as-grown surface without further polishing and annealing by electron microscopy and revealed a decreasing trend of grain size 6.1 μm to 4.2 μm. UV–Vis spectroscopy characterization ensured optical properties for bulk as well as nanopowders and the band gap has been found in the range of 1.4 to 1.6 eV and is increasing with Mg content. Magnetic hysteresis loop exhibits a less decreasing nature up to y = 0.3 of magnetic saturation along with the Law of Approach to saturation which compiles magnetic anisotropy. The temperature-dependent magnetization curves exhibit a sharp decreasing value (i.e. dM/dT minimum) at Curie point, decreasing from 630 K to 505 K with increasing Mg content. At 3 T magnetic field the changes in relative cooling power value have been found in the range 53.82 Jkg^{-1} to 37.79 Jkg^{-1} which could be considered as potential for magnetocaloric refrigeration. Impedance spectroscopy and other electrical characterization techniques were also employed to study the material's electrical properties. These measurements revealed that Mg^{2+} substitution improved the samples' electrical conductivity and dielectric properties. The findings of this research show the possibility of Mg^{2+} substitution as a strategy for tuning the structure, magnetic and electrical properties show the possibility of MLCI application in Ni-Cu-Cd bulk ferrite.

বিমূর্ত

অনুকূল ঘনত্বের সাথে বাল্ক সিরামিকগুলিকে তাদের ভাল চৌম্বকীয় স্যাচুরেশন, নিম্ন কোয়েরসিভিটি, এবং অ্যানআইসোট্রপি, বর্ধিত প্রতিরোধ, ইত্যাদির জন্য ডিভাইসগুলি তৈরি করতে ফেরাইট ন্যানো কণাগুলির তুলনায় অত্যন্ত অগ্রাধিকার দেওয়া হয়। $Ni_{0.5-y}Mg_yCu_{0.2}Cd_{0.3}Fe_2O_4$ ব্যবহার করে এই ধরনের বাল্ক নমুনা প্রস্তুত করতে 1423 K সিন্টারিং তাপমাত্রা এ গরম এবং শীতল করার হার যথাক্রমে 10 K এবং 5 K এ রেখে করা হয়েছে। এই বাল্ক নমুনাগুলি ব্যবহার করে কাঠামোগত পাশাপাশি তাত্ত্বিক Rietveld বিশ্লেষণ, অপটিক্যাল, ডাইইলেক্ট্রিক, তড়িৎ এবং চৌম্বকীয় বৈশিষ্ট্যগুলি বিশ্লেষণ করা হয়েছে। XRD স্ট্রাকচারাল বৈশিষ্ট্যগুলি অন্বেষণ এবং এই মানগুলি Rietveld Refinement পদ্ধতির সাথে বিশ্লেষণ করেছে এবং χ^2 (1-2) মান এবং অন্যান্য প্যারামিটার যেমন ল্যাটিস প্যারামিটার, ক্রিস্টাল স্ট্রাকচার, ক্যাটায়ন ডিস্ট্রিবিউশন এবং সর্বাধিক এনট্রপি ম্যাপিং এর ভালতা পেয়েছে। ইলেক্ট্রন মাইক্রোস্কোপির মাধ্যমে আরও পলিশিং এবং অ্যানিলিং ছাড়াই সারফেস আকারবিদ্যা এবং শস্যের আকার ক্রমবর্ধমান পৃষ্ঠ থেকে পরীক্ষা করা হয়েছে এবং শস্যের আকার 6.1 μm থেকে 4.2 μm হ্রাসের প্রবণতা প্রকাশ করেছে। UV-Vis স্পেকট্রোস্কোপি বৈশিষ্ট্য বাল্ক এবং সেইসাথে ন্যানোপাউডারগুলির জন্য অপটিক্যাল বৈশিষ্ট্য নিশ্চিত করেছে এবং ব্যান্ডের ব্যবধান 1.4 থেকে 1.6 eV-এর মধ্যে পাওয়া গেছে এবং Mg বিষয়বস্তুর সাথে বাড়ছে। চৌম্বক হিস্টেরেসিস লুপ চৌম্বকীয় স্যাচুরেশনের $y = 0.3$ পর্যন্ত কম হ্রাসকারী প্রকৃতি প্রদর্শন করে এবং সেই সাথে সম্পৃক্ততার পদ্ধতির আইন যা চৌম্বকীয় অ্যানিসোট্রপি সংকলন করে। তাপমাত্রা-নির্ভর চৌম্বকীয়করণ বক্ররেখাগুলি কুরি পয়েন্টে একটি তীক্ষ্ণ হ্রাসকারী মান (অর্থাৎ dM/dT সর্বাধিক) প্রদর্শন করে, ক্রমবর্ধমান Mg সামগ্রীর সাথে 630 K থেকে 505 K পর্যন্ত হ্রাস পায়। এ 3 T চৌম্বকীয় ক্ষেত্রে আপেক্ষিক শীতল শক্তির মান পরিবর্তনগুলি 53.82 Jkg^{-1} থেকে 37.79 Jkg^{-1} পরিসরে পাওয়া গেছে যা ম্যাগনেটোক্যালোরিক হিমায়নের জন্য সম্ভাব্য হিসাবে বিবেচিত হতে পারে। ইম্পিডেন্স স্পেকট্রোস্কোপি এবং অন্যান্য বৈদ্যুতিক বৈশিষ্ট্য কৌশলগুলিও উপাদানটির বৈদ্যুতিক বৈশিষ্ট্যগুলি অধ্যয়নের জন্য নিযুক্ত করা হয়েছিল। এই পরিমাপগুলি প্রকাশ করেছে যে Mg^{2+} প্রতিস্থাপন নমুনার বৈদ্যুতিক পরিবাহিতা এবং অস্তরক বৈশিষ্ট্যগুলিকে উন্নত করেছে। এই গবেষণার ফলাফলগুলি Ni-Cu-Cd বাল্ক ফেরাইটের মাইক্রোস্ট্রাকচার, চৌম্বকীয় এবং বৈদ্যুতিক বৈশিষ্ট্যগুলি টিউন করার কৌশল হিসাবে Mg^{2+} প্রতিস্থাপনের সম্ভাবনা দেখায়।

Table of Contents

Chapter 4: RESULTS AND DISCUSSION Page: 36

List of Figures

List of Tables

NOMENCLATURE

Symbol	Details
a_o	*Lattice constant*
D_{hkl}	*Crystallite size*
β	*Full width at half maximum*
ρ_x	*X-ray density*
ρ_B	*Bulk density*
R_p	*Profile R-factor*
R_{wp}	*Weighted profile R-factor*
R_{exp}	*Expected R-factor*
M_s	*Saturation magnetization*
H_c	*Coercive force*
μ_B	*Bohr magneton*
K	*Magnetic Anisotropy*
$\varepsilon^{/}$	*Dielectric constant*
$\varepsilon^{//}$	*Imaginary part of complex permittivity*
$M^{/}$	*Real part of electric modulus*
$M^{//}$	*Imaginary part of electric modulus*

CHAPTER 1
INTRODUCTION

Chapter 1: INTRODUCTION

1.1 BACKGROUND

The advantages of nanocrystalline ferrites have drawn a lot of attention because of their many special qualities, such as the formation of the core-shell structure at low temperatures and their high surface energy, which makes them dense at lower temperatures and significantly lowers the volatilisation cation and remain stoichiometric proportion. The scientific community and academics have been paying close attention to spinel-formed structural features in recent decades. These substances find utility as noise filters, multi-layered chip inductors, magnetic cores for recording discs, and other related applications [1]. The natural superlattice, closely packed by anions (O^{-2}), has created by the spinel cubic close-packed structure of the AB_2O_4 formula [2]. The magnetic, electrical, and structural properties of spinel cubic lattice are largely controlled by the substitution of non-magnetic ions. By adding a non-magnetic substance, the electrical and dielectric characteristics of the ferrite could be changed. For instance, Mg alters the structural characteristics of ferrites and exhibits observable alterations in cation distribution and magnetocrystalline structure when compared to a non-magnetic equivalent. They exhibit stronger saturation magnetization and lower coercivity characteristics of supermagnetic qualities [3]. Electronic devices including video cameras, laptop computers, and mobile phones frequently use NiCuZn-based MLCI [4]. Because Mg-Cu-Zn ferrite has a lower magnetostriction constant than Ni-Cu-Zn ferrite, the magnetic properties of MLCI using it would be higher [5]. Furthermore, magnesium-containing compositions are preferred because they inhibit the development of divalent iron, which is required for high resistivity, and the inclination toward discontinuous grain formation, which is required for dense ferrite [6]. Microwave appliances gain from these features. These ferrites also possess hard mechanical properties, a high Curie temperature, ecological stability, and affordability [7]. In order to achieve bulk dense ceramic by lowering certain restrictions and determining the uniform grain size distribution, the synthesis technique of nanoparticles is very important. With a straightforward, affordable, and energy-efficient process, it can be utilized to create high-purity chemicals at a low cost; in this study, nano ferrites are created using a sol-gel auto-combustion technique [8]. When bulk ceramics were made from nanocrystalline powders, a solidified material with uniformly fine grain over the range of densities was discovered [9].

Substituted ferrite exhibited a higher saturation magnetization than un-substituted ferrite regarding electromagnetic properties. Furthermore, the initial permeability of NiCuZn ferrite increased with substitution [10]. Diamagnetic ions substitution in spinel ferrites exhibits changes in their structural, electrical, and magnetic properties [11]. Due to Mg substitution, permeability improvements, dielectric loss reductions, and AC resistivity have all been seen in Ni-Cu-Zn ferrites [5].

Chavan et al. [12] produced $Ni_{1-x}Mg_xFe_2O_4$ at 1073 K via a solid-state reaction technique. The XRD (X-ray diffractometer) was used to confirm the structural formation of the ferrites. They also looked at the variations that resulted from the substitution of magnesium in nickel ferrite using various methods. They investigated saturation, remanent magnetization, lattice constant and porosity, and the characterization of electrical, optical, and magnetic properties.
P. K. Roy et al. [10] In order to create $Ni_{0.25-x}Mg_xCu_{0.2}Zn_{0.55}Fe_2O_4$, the sol-gel auto-combustion method was employed. X-ray diffraction (XRD) examination reveals an enhancement in the crystallite size, bulk density, saturation magnetization, and initial permeability caused by the diamagnetic Mg substitution of the sintered ferrite. Ferrites exhibited an increasing trend in bulk density with an increase in Mg content in NiCuZn, which led to a decrease in porosity. In terms of magnetic characteristics, substituted ferrite showed a greater saturation magnetization (M_s) than unsubstituted ferrite. Moreover, with the substitution of Mg, the initial permeability of NiCuZn ferrite increased. Spinel ferrites with diamagnetic ion substitution show modifications in their structural, electrical, and magnetic characteristics. [11].

R. Valenzuela et al. [13] Bulk ceramics are preferred over nanocrystalline powder samples in electronic and microwave applications because these Confining polycrystalline solids within the 200 nm region are advantageous in electronic and microwave applications.

M. Moazzam et al. [3] published from our lab, where XRD verification of the effectively produced NMCC nanoparticles was obtained. Up to a decrease in coercivity and a y = 0.3 Mg concentration, Ms is nearly constant.

With an affinity for the A site in the crystal lattice, Cd and Zn share comparable characteristics. NiCuCd containing Cd exhibits several advantageous characteristics,

including low eddy current and dielectric losses, high resistivity, intrinsic magnetic hysteresis, and high crystallinity [7].

1.2 AIMS AND OBJECTIVES

NMCC are chosen in the in the exception aiming of having at least one of the following properties:

- good χ^2 fitting value by using Rietveld Refinement technique.
- adequate saturation magnetization
- good optical bandgap value
- maximum initial permeability
- minimum losses
- analysis of transport behavior by impedance and modulus spectroscopy
- finally but by no means the least important, minimum cost etc.

The main objectives of the present research are as follows:

- Synthesis of $Ni_{0.5-y}Mg_yCu_{0.2}Cd_{0.3}Fe_2O_4$; ($0.0 \leq y \leq 0.5$, step size 0.1) nanoparticles and are used to make bulk disc and toroid form specimens, which are sintered at 1150°C.
- XRD data have been used to characterize the structural properties of various composition.
- The density and porosity of all composition would be determined from the sintered specimen and XRD data.
- Study of the surface morphology and microstructure.
- Magnetic hysteresis parameter by measurement by PPMS and initial permeability spectra by impedance analyzer.
- The frequency-dependent dielectric and electric features of every composition have explored.
- Analysis of impedance and modulus spectroscopy have done with the connection of theoretical approach.

Possible outcome of the research is as follows

The homogeneous nanocrystalline powders are projected to produce bulk ferrites. In terms of microstructures, initial permeability, saturation magnetization, electric, dielectric characteristics, grain, and grain boundary resistances, there would be a lot of interest in the synthesis of uniform magnetic nanocrystals with adjustable size and superior quality materials. Scientists and technologists were be able to use the findings to fabricate a variety of devices employing these ferrites.

1.3 THESIS OUTLINE

Chapter 1: The "*INTRODUCTION*" chapter includes an overview of the research for the research problem statement, rationale for the investigation, the goals and scope of the study, and potential outcomes.

Chapter 2: The "*LITERATURE REVIEW*" chapter covered the theoretical underpinnings of the current research paradigm as well as a summary of some previously published work.

Chapter 3: The "*MATERIALS AND METHODOLOGY*" chapter includes the synthesis of the prepared samples and a brief overview of various characterization techniques, including XRD, Impedance Spectroscopy, PPMS, UV-vis spectra, etc.

Chapter 4: The "*RESULTS AND DISCUSSION*" chapter presents the findings of this investigative project and interprets the findings using existing theories.

Chapter 5: The "*CONCLUSIONS*" chapter contains some key findings from the overall experimental data as well as some recommendations for further study.

Finally, a brief list of conferences and publications that are linked to the current research.

CHAPTER 2

LITERATURE

REVIEW

Chapter 2: LITERATURE REVIEW

2.1 GENERAL

This section provides a thorough summary of the research, including the thesis's primary topic, which will be discussed in the literature review. Key research papers will be included here, along with their methodologies, conclusions, and contributions to the field.

2.2 FERRITES

Ferrites are a well-known type of ferrimagnetic materials with a naturally occurring super lattice structure made up of various iron oxide combinations. Hematite (Fe_2O_3), magnetite (Fe_3O_4), and other metal oxides like NiO, CuO, etc. are a few examples of ferrites that are well-known. $M^{2+}Fe^{3+}{}_2O_4$ is the general formula for ferrite, where M^{2+} is a divalent metal ion. This M^{2+} ion can be swapped out for Mn^{2+}, Co^{2+}, Cu^{2+}, Mg^{2+}, Zn^{2+}, or Cd^{2+}. Because ferrites have a dc resistivity nearly 10^4–10^{11} times higher than iron, they can be used in high-frequency applications.

2.2.1 CLASSIFICATIONS

Based on a variety of characteristics, ferrites can be categorized into several groups. These are a few of them. Ferrites fall into one of two groups based on their magnetic coercivity:

a) SOFT FERRITES

Soft ferrites are easily magnetized, and the opposite is also true. This clearly shows that soft ferrites have high magnetization and a low coercive field. These qualities are necessary for a lot of electrical applications. In soft ferrites, the hysteresis loop appears to be quite thin. These materials have strong magnetic permeability and extensive temperature stability.

b) HARD FERRITES

After the magnetizing field is removed, hard ferrites exhibit magnetization polarity. Because of this, these strong remanence ferrites are known as permanent magnets.

Conversely, ferrites can be divided into four groups based on their magnetic ordering and crystal structure: Spinel-ferrite, Garnet, Hexa-ferrite and Ortho-ferrite.

Table 2.1: The fundamental distinctions between the four ferrites.

Types	*Structure*	*General Formula*	*Examples*
Spinel	*Cubic*	$A^{II}Fe_2O_4$	A^{II}=Mg, Co, Zn, Ni, Cd
Garnet	*Cubic*	$Ln_3{}^{III}Fe_2O_{12}$	(Ln^{III}=Y, Sm, Eu, Gd, Er
Hexa-ferrite	*Hexagonal*	$M^{II}Fe_{12}O_{19}$	$BaFe_{12}O_{19}$
Ortho-ferrite	*Perovskite*	$LnFeO_3$	Ln=similar as garnets

2.2.2 SPINEL FERRITES

The most significant ferrite structure from a technological standpoint is seen in spinel, particularly in the electronic device industry. Bragg and Nisikawa made the first determination of spinel structure in 1915 [14, 15]. Both trivalent and divalent cations are present in soft ferrites with an FCC closed-packed spinel crystal structure [16]. The formula for spinel ferrites is $[A][B]_2O_4$. Divalent metal ions prefer the tetrahedral A-sites, while metal ions with valency 3 prefer the octahedral B-sites. Anions are closely packed and one-eighth of the cations in the ideal spinel structure are occupied in the A-site interstices, while the other half of the cations are occupied in the B-site interstices. Fd-3m is the most abundant space group in crystalline spinel among other space groups. The structure of spinel structure is showed in Fig. 2.1.

2.2.2.1 TETRAHEDRAL SITES

The four lattice anions encircle the interstitial in tetrahedral locations. Of these four anions, three are in contact with one another in the same plane, and the fourth is symmetrically positioned at the top above the atoms that are in the middle. The cation is located in the middle of the empty space that has been produced. In the crystal structure of FCC, cations occupy just eight A-sites out of 64 sites in each unit cell. Fig. 2.2(a) depicts the tetrahedral A-sites pictorially.

2.2.2.2 OCTAHEDRAL SITES

The six lattice anions encircle the interstitial in octahedral sites. Of these six anions, two are symmetrically positioned at the top and bottom corners of the centered atoms, and four are in the same plane, touching one another.

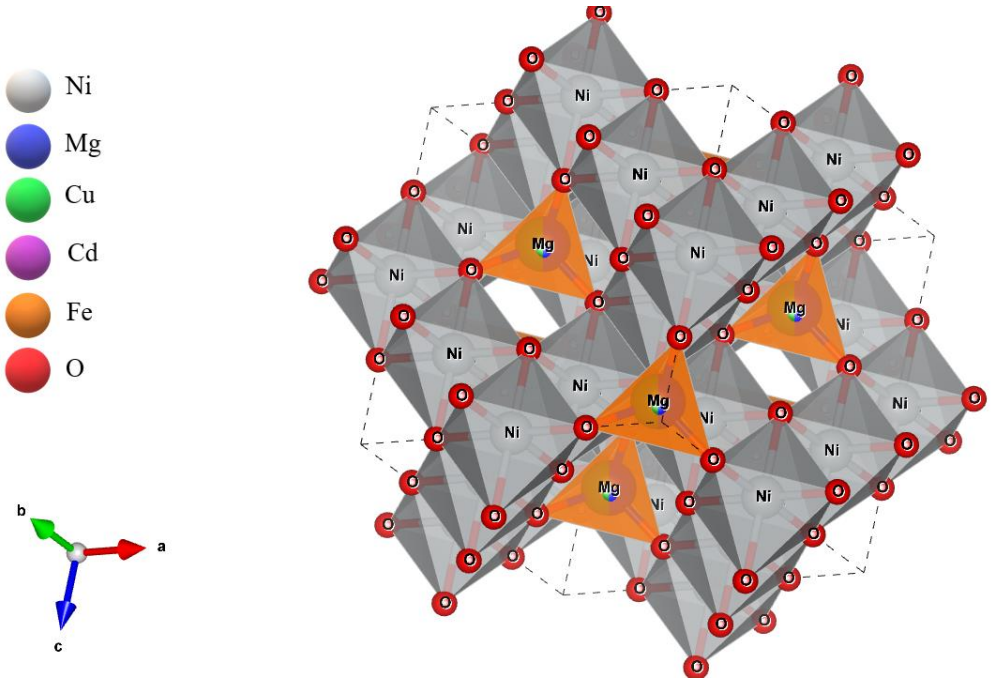

Fig. 2.1 Spinel structure

The center of the generated void is where the cation is located. Cations only occupy 4 A-sites out of 32 sites in each unit cell in the FCC crystal structure for charge neutrality. Fig. 2.2(b) displays an illustration of octahedral B-sites.

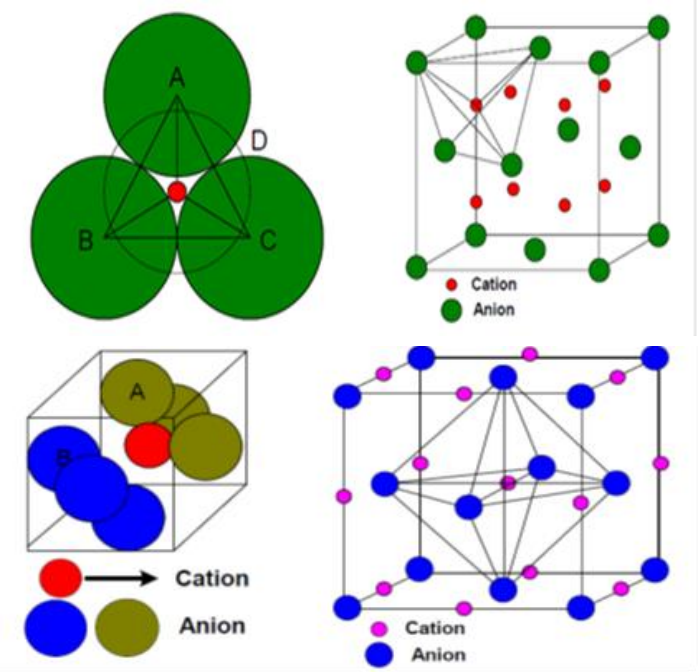

Fig. 2.2 (a) Tetrahedral A-site and (b) Octahedral B-site

2.2.2.3 SPINEL FERRITES ACCORDING TO CATION DISTRIBUTION

Based on the distribution of cations on A- and B-sites, the spinel ferrites are divided into three groups. These are listed in the following order:

a) Normal spinel structure b) Inverse spinel structure c) Mixed spinel structure

a) NORMAL SPINEL

Normal spinel structure is defined as all trivalent cations going to the B-sites and all divalent cations going to the A-sites. $(Me^{2+})[Fe_2^{3+}]O_4^{2-}$ is the general formula for typical spinel ferrites. The illustration below shows the distribution within the typical spinel structure.

(A) [B]

$$(Me^{2+})[Fe_2^{3+}]O_4^{2-}$$

b) INVERSE SPINEL

The structure is called an inverted spinel structure if all of the divalent metallic cations move to the B-sites and the trivalent cations are evenly distributed in both sites. For the inverse spinel ferrites, the typical formula is $(Fe^{3+})[Me^{2+}Fe^{3+}]O_4^{2-}$. Below is an illustration of the distribution in the inverse spinel structure:

(A) [B]

$$(Fe^{3+})[Me^{2+}Fe^{3+}]O_4^{2-}$$

c) MIXED SPINEL

A mixed spinel structure is one in which both divalent and trivalent cations are dispersed throughout both sites. For mixed spinel ferrites with δth degree of inversion, the typical formula is $(Me_{1-\delta}^{2+}Fe_{\delta}^{3+})[\,Me_{\delta}^{2+}Fe_{2-\delta}^{3+}]O_4^{2-}$. The illustration below shows the distribution within the typical spinel structure.

(A) **[B]**

$$(Me^{2+}_{1-\delta}Fe^{3+}_{\delta})[\,Me^{2+}_{\delta}Fe^{3+}_{2-\delta}]O^{2-}_{4}$$

2.3 APPLICATION OF FERRITES

Soft ferrites are one of the two types of ferrites that are most commonly used in transformer cores for electronic systems such as television, computers, medical equipment, and telephones because they are easily magnetized and demagnetized. Moreover, a second variety of ferrites called hard ferrites is difficult to demagnetize but, once magnetized, can be employed in permanent magnets like those found in loudspeakers and micromotors. For high frequency applications, polycrystalline ferrites with a low loss factor make suitable choices. Their M_S, coercive force (H_C), initial permeability (μ_i), losses, and other significant characteristics make them perfect for both low- and high-frequency technical applications. By simply adjusting the compositions by the addition of additives or different preparation techniques, it is simple to obtain the best possible mix of these qualities for any given application. Based on the specific application, most of these factors are controllable to some extent. Ferrites are also useful for the purposes listed below:

- Inductors
- High frequency devices
- High-density write-once optical recording
- Magnetic sensor
- Magnetic shielding
- Ferrite as electrodes
- Multi layered chip inductors
- Magnetocaloric effect

2.4 REITVELD REFINEMENT

Rietveld refinement is a crucial instrument for crystalline material characterization [17]. The X-ray diffracted powders' reflection-based pattern characterization can be improved to yield specific parameters, including peak height, peak width, and the location of these reflections at different intensities. These parameters are highly valuable for a range of material structural studies. Unless the measured profile matches the measured profile well, the rietveld method refines a line produced from the theoretical profile using a least squares approach [18]. The figures of merit that are used to describe the refining quality are as follows.

a) GOODNESS OF FITTING

The most significant parameter that represents the refining outcome is called goodness of fit, and it is represented by the symbol $\chi 2$. The $\chi 2$ can be derived using the accompanying formula;

$$\chi^2 = (\sum_i^n ((Y_i^{obs} - Y_i^{calc})^2 / (n-p)) = R_{wp}/R_{exp}$$

b) PROFILE RESIDUAL

A refining process's profile residual, or dependability factor, can be expressed as follows;

$$R_p = \sum_i^n (|Y_i^{obs} - Y_i^{calc}|/\sum_i^n Y_i^{obs})\times 100\%$$

Y_i^{obs} represents the intensity profile that is observed, Y_i^{calc} represents the profile intensity that is calculated at the ith point, and n represents the total number of data points.This yields the weighted residual profile;

$$R_{wp} = (\sum_i^n (\omega_i (Y_i^{obs} - Y_i^{calc})^2 / \sum_i^n \omega_i (Y_i^{obs})^2)^{1/2}\times 100\%$$

For where the weight is ω_i. The profile of the Bragg residual is as follows;

$$R_B = \sum_j^m (|I_j^{obs} - I_j^{calc}|/\sum_i^n I_j^{obs})\times 100\%$$

The integrated intensities of the j^{th} observed and measured Bragg peak are denoted by I_j^{obs} and I_j^{calc}, respectively. The predicted residual profile can be found using;

$$R_{exp} = ((n-p) / \sum_i^n \omega_i (Y_i^{obs})^2)^{1/2}\times 100\%$$

where the phase is indicated by p.

2.5 DENSITY

Measured in ions, atoms, or molecules per unit volume of the crystal structure, the density of the substance is determined. In order to optimize the real density analysis, many computations using various formulas were performed for the detailed investigation of density. The following formula is used to determine the compound's bulk density;

$$\rho_B = M/V$$

This represents the specimen's mass (M) and volume (V). Two distinct formulas were used to compute the volume of the specimen in the disc and toroid shapes. Using the formula below, one may determine the volume of the toroid or ring-shaped specimen.

$$V = \pi(R_{out}{}^2 - R_{in}{}^2)\, h$$

where π is a constant equal to 22/7, R is the radius of the disc, h is the thickness of the sample, and R_{out} and R_{in} are the outer and inner radii of the ring.

The amount of void space in a compound structure is measured by its porosity. The values derived from the density measurement can be used to determine the porosity of each chemical. So, the porosity is determined in the manner shown below,

$$P(\%) = \{(\rho_{th} - \rho_B)/\rho_{th}\} \times 100\%$$

The parameter that affects both the bulk ceramics' electromagnetic and structural properties is density. The ρ_{th} is determined by the molecular weight and ionic radius of the A- and B-site cations.

2.6 MAGNETISM

A magnetic moment results from an electron's intrinsic spin. The magnetic particles are categorized as diamagnet, paramagnet, ferromagnet, and antiferromagnet based on the presence of the magnetic moment. In 2.3, every kind of magnetic substance is represented,

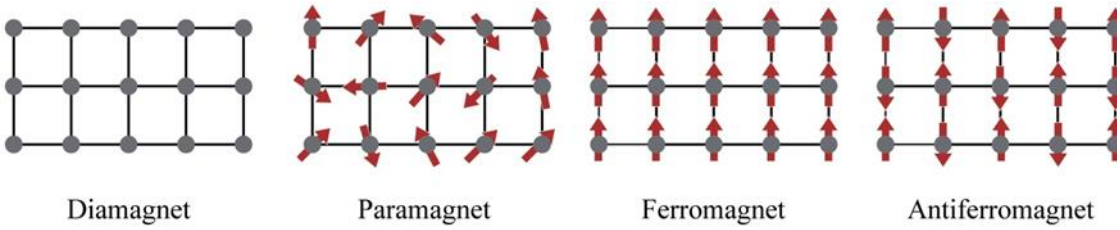

Fig. 2.3 Criteria of magnetic materials

There is no magnetic moment in a diamagnet. Every atom in a paramagnet has a magnetic moment, but these interactions are not very strong. While nearby atoms interact intensely with one another in ferromagnets and antiferromagnets, their magnetic moment directions are opposing. Only the ferromagnet, which is aligned in the same direction as the other magnetic particles, has a magnetic moment.

2.6.1 DOMAINS

Anything composed of magnetic domains. Domains are often bigger than atomic sizes, ranging from 1 to 100 microns. Single domain formation occurs when a large single crystal is continuously magnetized. A magnetic field is created as a result of surface charges forming as a result of the magnetization. The energy associated with the distribution of surface charges is the source of magnetostatic energy. This magnetostatic energy can be divided into two domains, the (+) and (-) charges, which are magnetized in opposing directions. It is not possible to split into more domains because doing so would demand more energy to construct and maintain. The equilibrium number of domains is almost fixed for a given particle size. Measure the domain wall width by magnetocrystalline energy exchange.

2.6.2 MAGNETIC SATURATION

Saturation Magnetization (M_S) of a ferromagnetic material is the maximum magnetization that can be generated in an external field and occurs when all of the magnetic dipoles in a solid piece are mutually aligned with the external field.

$$M_S = \frac{magnetic\ moment\ per\ atom \times density \times Avogadro's\ number}{Atomic\ weight}$$

Magnetic ferrites, like ferromagnetic materials, also have magnetic domain structures; in the ferrites, magnetization originates from each domain like with the present individual ions, and strong quantum mechanical forces originate from the interaction of spinning electrons in the neighboring metal ions.

2.6.3 MAGNETIC ANISOTROPY

Magnetic materials inherently have a propensity to align their magnetic moments with one of the main crystal orientations. The preferred magnetization direction is this orientational direction. Ferrimagnetic and ferromagnetic materials exhibit magnetization along a set of crystal directions [20]. Multiple factors can lead to anisotropy in a magnetic material. Shape and magnetocrystalline anisotropy are the two most significant types of anisotropies available. Magnetocrystalline anisotropy is produced by the system's crystal symmetry, while form anisotropy is generated by the magnetized body's geometrical shape. Stresses imposed by mechanics produce the third anisotropies.

2.6.4 HYSTERESIS LOOP

A magnetic substance does not return to zero magnetization after the imposed magnetization is removed. In order to drive it to zero, a negative field must apply. When a material is subjected to an alternating magnetic field, its magnetization will form what is known as a hysteresis loop. Fig. 2.4 shows an example of a typical magnetization versus applied magnetic field graph. The persistence of magnetic domains inside the material is connected to the hysteresis loop. It took considerable energy for the magnetic domains to revert to their original orientation after they had done so. The magnetic memory properties of iron oxides are particularly useful for recording audio on tape and storing data magnetically on computer drives. When a material is demagnetized, its spins are randomly orientated, and any linked magnetic fields cancel each other out to produce a magnetic field that is zero. Because ferromagnetic materials have a lower energy configuration, there are many different types of magnetic domains. Magnetization flips are referred to as domain walls at the boundary between two domains. When the ferromagnet material is exposed to an external magnetic field, the domains within the sample enlarge at the boundary of the neighboring domain, which is approximately perpendicular to the applied field. This phenomenon is identified as a motion of the domain wall.

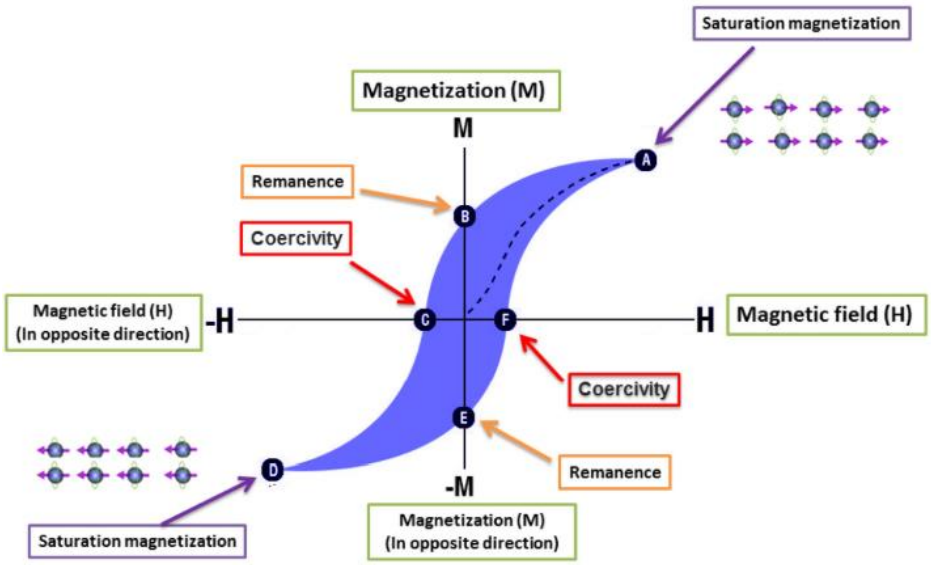

Fig. 2.4 Magnetic hysteresis loop [7]

2.7 DIELECTRICS

Dielectric electrical insulators are those in which there is no free charge and all atoms are confined by their nearest counterparts. An external electric field causes the electron cloud center to slightly separate, and it also causes the ion's positive core to act as an electric dipole.

2.7.1 DIELECTRIC PROPERTIES

2.7.1.1 DIELECTRIC POLARIZATION

Applying an electric field to a dielectric material will cause the distribution of already-existing dipoles to change, which will lead to the production of new dipoles. Dielectric polarization is the name given to this phenomenon. Polarization is defined as the electric dipole moments per unit volume. When a molecule is in an electric field, its electric moment is proportional to the applied field. Polarization P is determined by,

$$P = N\alpha E$$

where N, α, and E stand for the electric field, polarizability, and number of atoms, respectively.

2.7.1.2 COMPLEX DIELECTRIC CONSTANT

The capacitance of the material-filled capacitor (C) divided by the capacitance of the vacuum capacitor (C_0) is the definition of relative permittivity. It is comparable to air for both liquids and solids. It is also known as the dielectric constant and specific inductive capacity. It is an electrical material's insulating property. It reveals large-scale dielectric properties for the atomic scale rather than fixed electrical behavior.

$$\varepsilon = C/C_0 \qquad \text{where, } C_0 = \varepsilon_0 A/d$$

The material's dielectric constant is a measurement used to express how much polarization it can withstand in an applied field. The four categories of polarizing sources are space charge, dipolar charge, atomic charge, and electronic charge. The latter two varieties have an impact on the material at the microstructure scale of ferroelectric materials, while the former two types have no discernible effect. One way to express the frequency-dependent complex dielectric constant is as [21]

$$\varepsilon^* = \varepsilon' - j\varepsilon''$$

The real part of the dielectric constant (ε') represents the stored energy, and the complex part of the dielectric constant (ε'') represents the dissipated factor. These two terms are combined in the equation above. The following describes how they are connected to the capacitance measurements of capacitors,

$$\varepsilon = C_p d/\varepsilon_0 A$$

Where, A is the pellet's cross-sectional area, d is the thickness of the pellet, ε_0 is the free space permittivity where magnitude is 8.854×10^{-12} $C^2N^{-1}m^{-2}$ and Cp stands for the pallet capacitance.

2.7.1.3 DIELECTRIC LOSS TANGENT

The dielectric loss tangent is the ratio of energy wasted to energy consumed. It is said as follows:

$$\varepsilon'' = \varepsilon' \tan\delta \qquad \text{or, } \tan\delta = \varepsilon''/\varepsilon'$$

The dielectric loss tangent (tanδ) [22] is influenced by compositional dependency factors, specifically structural homogeneity, stoichiometry, and ferrous concentration. It also depends on the sintering temperatures.

2.7.2 COMPOSITION AND FREQUENCY DEPENDENCY OF DIELECTRIC CONSTANT

a) COMPOSITION

In ferrites, έ is influenced by a number of microstructure and structural variables. It is discovered that έ rises with increasing Cu content in the case of Ni-Cu-Cd ferrites. Furthermore, Ni travels to the B-sites whereas CD visits the A-sites. However, Fe^{2+} and Fe^{3+} have the ability to occupy both A- and B-sites. When a small amount of Fe^{3+} is substituted with Cu, some of the Fe^{3+} has been converted to Fe^{2+}, maintaining the neutral charge. Consequently, the rising Fe^{3+} and Fe^{2+} hopping indicates that the grains are diminishing. Thus, electrons have a higher chance of entering the grain border. As a result, polarization and dielectric constant have both risen.

b) FREQUENCY

The change in ε′ with frequency is dependent on different polarizations. When the frequency increases, ε′ begins to decrease, but at low frequencies, it has a very high value. At high frequencies, it becomes excessively tiny, similar to frequency independence. Two-layer model by Maxwell and Wagner [23] is a very useful tool for explaining ε′ variance. This concept states that the insulating matrix or grain borders and the highly conductive phase or grain in between them make up the structure of the dielectric materials [24]. Because of the material's heterogeneous nature, space charge polarization has been created. An external ac electric field is applied at the grain boundaries, causing local charge accumulation [25]. Electrons clump together near the grain border due to its high resistance, which results in polarization. The time it takes for space charge carriers to align with the alternating field is finite. Unfortunately, when the frequency of the reversal field rises, these carriers are not able to reach the direction of the electric field because of the absence of charge carriers in the grain boundary. Carriers flow in a direction that is behind the direction of the external field as a result. As polarization diminishes due to a reduction in charges at the grain boundaries, ε′ likewise lowers. Therefore, a further rise in field frequency causes space charge carriers to transition ahead of the reversal field, meaning that dielectric materials do not contribute to polarization. It was noted that the polarization mechanism is comparable to conduction in the ferritin situation. The electronic displacement of the applied field direction is caused by the polarization, which is established by the $Fe^{2+} \rightarrow Fe^{3+}$

exchange. The larger value of ε can be attributed to the prevalence of certain species, such as Fe^{2+}, oxygen vacancies, voids, grain boundary defects, interfacial dislocation pile ups, and so on [26]. Therefore, the decreasing trend of έ is consistent with the rising incidence of polarizing species delaying their activities.

2.8 MODULUS SPECTROSCOPY

An important technique for analyzing the dielectric properties of polymeric insulators is the complex electric modulus. It is useful when high temperatures cause complicated permittivity to increase in value. This high complex permittivity value at this point is caused by electrode polarization and carrier movement. The complex electric modulus can be used to measure dielectric properties at high temperatures since it is reciprocal to the complex permittivity. The real part ($M^{/}$) with the imaginary part ($M^{//}$) together form the complex electric modulus, which is shown as follows,

$$M^{*} = M^{/} + jM^{//}$$

The following describes how these terms relate to the corresponding dielectric constant and impedance components [27],

$$M^{/} = \varepsilon^{/}/(\varepsilon^{/2} + \varepsilon^{//2}) \;=\; \omega\, C_o\, X$$

$$M^{//} = \varepsilon^{//}/(\varepsilon^{/2} + \varepsilon^{//2}) \;=\; \omega\, C_o\, R$$

where f and X stand for the linear frequency and angular frequency, respectively, and X and R for reactance and resistance.

2.9 IMPEDANCE SPECTROSCOPY

Impedance is a phenomenon that arises from the proportion of voltage to current in the frequency domain. The ratio between the amplitudes of the voltage and the current can be used to express the complex impedance. We refer to the complex impedance phase as the reverse phase shift of current to voltage. In polar form, the complex impedance can be written as,

$$Z^{*} = |Z|\, e^{j\, arg\,(Z)}$$

The phase difference between the voltage and the current is represented by arg. (Z), where |Z| is the magnitude of the amplitude of the voltage ratio to the current. The

expression for the complex impedance of the dielectric medium in ferroelectrics is as follows: it is the sum of the reactance and resistance,

$$Z^* = R + jX$$

Impedance or reactance's complex component is represented by X, while its real part is marked by R. The phase shift θ for these two quantities is given by,

$$R = |Z^*| \cos\theta \qquad and \qquad X = |Z^*| \sin\theta$$

Impedance spectroscopy is essential for examining the electrical characteristics of ceramic materials.

2.10 PREVIOUS WORK ANALYSIS

A brief discussion of some of the literatures that inspired this study is provided below;

2.10.1 SYNTHESIS OF NCC FERRITES

Spinel ferrites are created via a variety of methods, including co-precipitation, hydrothermal, solid-state reaction, and sol-gel auto combustion.

Many researchers had used the sol-gel auto combustion approach to manufacture Ni-Cu-Cd [27, 28]. The same techniques were used to manufacture other spinel ferrites, such as Ni-Cu-Zn [25, 29 – 31], Ni-Zn [32], Cu-Co [20], etc., in addition to the Ni-Cu-Cd ferrites. In general, this process uses metal nitrate salts as reactants and includes fuel for the auto-combustion reaction. Ammonia [23, 29], citric acid [33, 34], urea [35], and glycine [36] are the fuels that are most frequently used. Ammonia is better than other substances since it speeds up the reaction more. While using citric acid helps lessen the excess pollution from N_2 gas, it also slows down the rate of reaction, which has an impact on the synthesized chemical. The scientific community has mainly acknowledged this technology for ferrites synthesis due to its ease of use and affordability [37]. Nano-structured ceramics have provided novel properties. In these ceramics, the sintering process increases surface area, which results in a decrease in free energy. When the temperature of the particle sintering is lower, the main driving force is the increased surface area. The ideal particle size can optimize a variety of desired sectors' attributes, such as mechanical, optical, electrical, thermal, and so forth [38]. The transition of the materials into the nano range has significantly altered their characteristics. However, this conversion results in a drop in the particle density.

Consequently, these ceramics lost their suitability for use in certain equipment that calls for high density ceramics. Because of their higher density, regular bulk ceramics can be taken into consideration; but, because of their larger crystal sizes, the desired qualities are still out of reach. Because dense ceramics have a high density and a nanometric range, they have been created specifically for these kinds of procedures. Numerous research projects have examined the value and uses of solid ceramics [39, 40].

However, in other studies, solid state reaction techniques have been employed to create nickel-based ferrites [41, 42]. Using this procedure, several metal oxides are combined through grinding and calcined to produce ceramic ferrites. This mechanical mixing is very difficult to control, and there have been fluctuations at every preparation step that might not go away after sintering. Furthermore, the high temperature needed for calcinations in this approach may result in the evaporation of some metal ions, which ultimately leads to flaws in the produced products. A further technique for creating spinel ferrites specimens is co-precipitation [43, 44]. For the most part, this approach of creating nanocrystalline ferrite ceramics is economical and time-consuming. This method's intriguing benefit is its ability to produce specimens with a wide variety of crystallite sizes in all dimensions [45]. The most recent technique for creating nanoparticles is the hydrothermal approach [46]. The synthesis in this procedure makes use of the hydro thermal effect. The cavity and other tools required for this process come at a high cost. Moreover, the procedure is extremely dangerous because the generated molecule is often damaged because the generation is not detected in a timely manner. The chemical synthesis technique requires several modes of operation that take a long time, as well as the pricey and extremely sensitive alkoxide precursor [47] that is needed for the synthesis, which necessitates further concentration. Sol-gel auto combustion, on the other hand, has advantages over chemical procedures due to the need for inexpensive equipment, a lower energy consumption, and homogenous, highly reactive, nanosized results. The structural, magneto-electric, and dielectric characteristics of the ferrite samples can be changed by substituting a tiny nonmagnetic element, like magnesium, which can also change the magnetocrystalline anisotropy and cation distribution. Relative coercivity varies along with the addition of magnesium, much as the magnetocrystalline anisotropy does. Super magnetic characteristics including reduced coercivity and strong saturation magnetization are displayed by these ferrite materials. Mg-based ferrites have garnered attention recently because of their

low dielectric losses and high electrical resistivity [48]. In microwave devices, these qualities are advantageous. In addition to having high Curie temperatures, ecological stability, and hard mechanical qualities, these ferrites are also incredibly inexpensive [49].

H. Moradmard et al. [50] artificial Nickel ferrite nanopowders doped with magnesium were made using the co-precipitation method, and all samples were annealed at 900ºC. They discovered that the saturation magnetization dropped when magnesia took over. All of the ferrite samples' structural, magnetic, and dielectric characteristics were also investigated.

R. M. Rosnan et al. [51] $Co_{0.5}Ni_{0.5-x}Mg_xFe_2O_4$ was effectively synthesized using the co-precipitation method. As the magnesium content increased, they saw an increasing trend in the lattice constant, magnetism, and coercivity.

B. Thangjam and I. Soibam [52] $Ni_{0.5-x}Mg_xCu_{0.3}Zn_{0.2}Fe_2O_4$ was successfully synthesized using the traditional citrate precursor process, where x=0.05, 0.10, 0.15, and 0.20. At room temperature, they noted high resistivity values, minimal dielectric loss, and low dielectric constant.

Pradeep et al. [53] $Ni_{1-x}Mg_xFe_2O_4$ produced with the use of the solid-state reaction process. The impact of replacing the magnesium ion in nickel ferrite on the crystallite size, lattice constant, porosity, binding nature of materials, conduction mechanism, Curie temperature, activation energy, drift mobility variation as a function of temperature, dielectric relaxation, bandgap energy, magnetic moment, saturation magnetization, and remanent magnetization has all been investigated.

S. M. Kabbur et. al. [54] Using glycine as fuel, a sol-gel auto-combustion process produced a $Ni_{0.25-x}Mg_xCu_{0.30}Zn_{0.45}Fe_2O_4$ magnetic oxide system. They found that when the Mg^{2+} content increased, the lattice constant, magnetic moment, and Curie temperature all trended downward. They examined the infrared (IR) spectroscopy's intrinsic vibrational absorption bands.

CHAPTER 3

MATERIALS

AND

METHODOLOGY

Chapter 3: MATERIALS AND METHODOLOGY

3.1 RAW MATERIALS AND SYNTHESIS OF NANOPARTICLES

$Ni(NO_3)_2 \cdot 6H_2O$, $Mg(NO_3)_2 \cdot 6H_2O$, $Cu(NO_3)_2.3H_2O$, $Cd(NO_3)_2.4H_2O$, and $Fe(NO_3)_3.9H_2O$ have been used as raw materials. To synthesize $Ni_{0.5-y}Mg_yCu_{0.2}Cd_{0.3}Fe_2O_4$ ($0.0 \leq y \leq 0.5$, step size 0.1), nano ferrites sol-gel synthesis technique has been implemented. The stoichiometric raw materials have been dissolved in ethanol and mixed to form a homogenous solution. The magnetic stirrer has continuously agitated the following solution for 2 hr. The required quantity of liquid ammonia has been added inwardly to the solution to keep the pH 7 at a predefined level. Then the solution was placed at a temperature of 353 K in a water bath to form a dried gel. It has taken 24 hr to homogenize in equilibrium. Following the dried gel, they have been heated in the oven at 473 K for 5 hr to turn them into fluffy loose powder. Samples have been annealed for 5 hr at 973 K to ensure stable crystallinity. The production process has finally yielded NMCC nano ferrites as a fluffy powder.

3.2 PREPARING BULK SPECIMENS

The following ferrite powder then has been hand-milled for 2 hr vigorously to form fine homogeneous particles. To granulate the powder, the proper amount of polyvinyl alcohol (PVA) has been added. The hydraulic press machine has been used to press the granulated ferrites to form the samples' desired disc and toroid-shaped samples. The disc and toroid samples have been pressed with a pressure of 600 psi for two minutes. After that, the specimen has been kept for sintering at 1423 K in the furnace for 5 hr. The samples have been first used to observe surface morphology images and then polished with sandpaper to make them suitable for the other experiment. Fig. 3.1 illustrates the synthesis procedure.

3.3 STRUCTURAL ANALYSIS USING XRD

3.3.1 X-RAY DIFFRACTION

X-ray diffraction (XRD) is an effective technique for conducting structure analysis and phase identification of a broad range of substances, including metals and composites, polymers and biological materials, and electronic and optoelectronic substances.

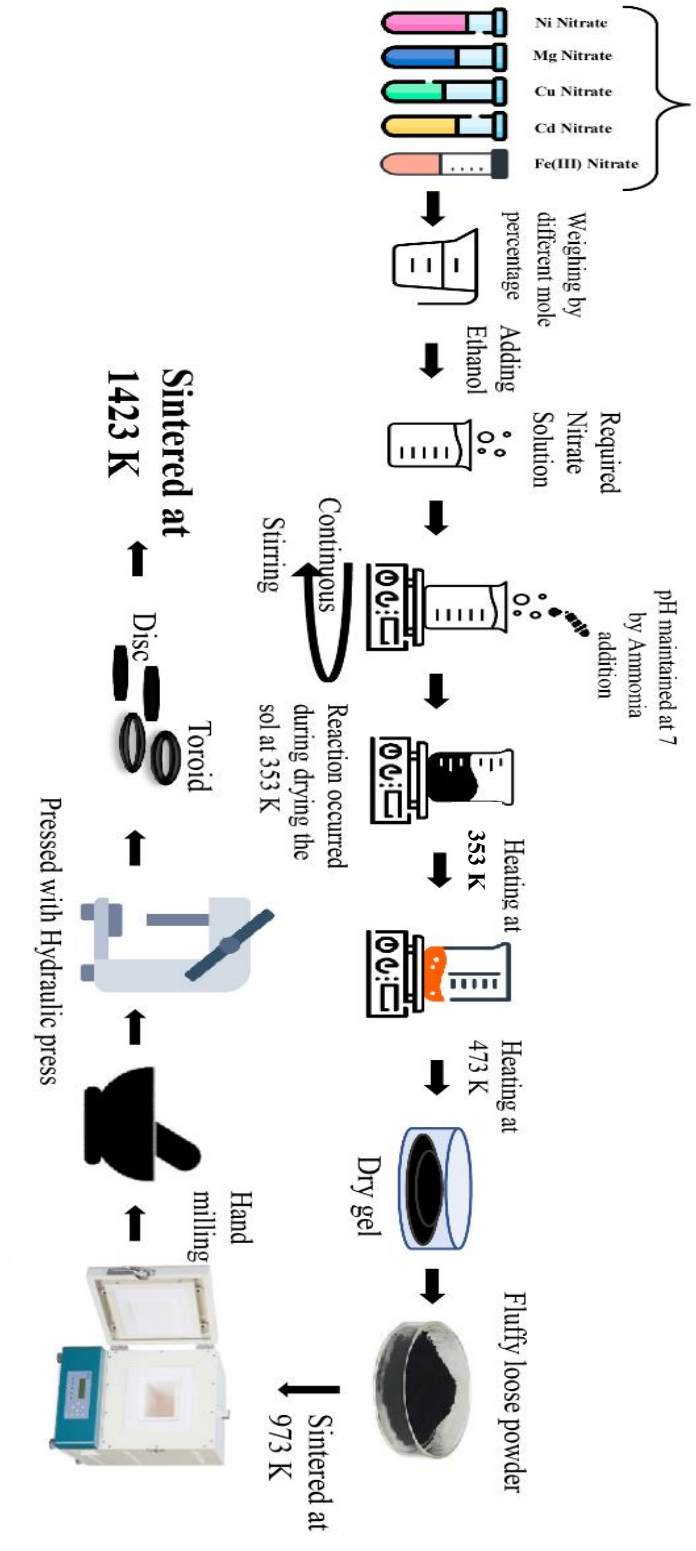

Fig. 3.1 Synthesis technique for NMCC ceramic preparation

Because the wavelength of X-rays is comparable to the size of an atom, they can be used to obtain information on the atoms and molecules of ferrite materials. Following an X-ray's incidence on a ferrite material, an electron-atom collision and scattering happen. This collision sturdily changed the resulting intensity that is the summation of all the diffracted waves that comes from various atoms. This diffracted wave gives sharp interference maxima analogous to the allocation of the atoms in crystals. These peaks are directly related to atomic distances. Fig. 3.2 shows the incidence of X-rays on the atoms as they happen. The atoms that make up the various plane sets in the crystal are represented by the circles. A set of planes' diffraction peak can be reached by using Bragg's law [55].

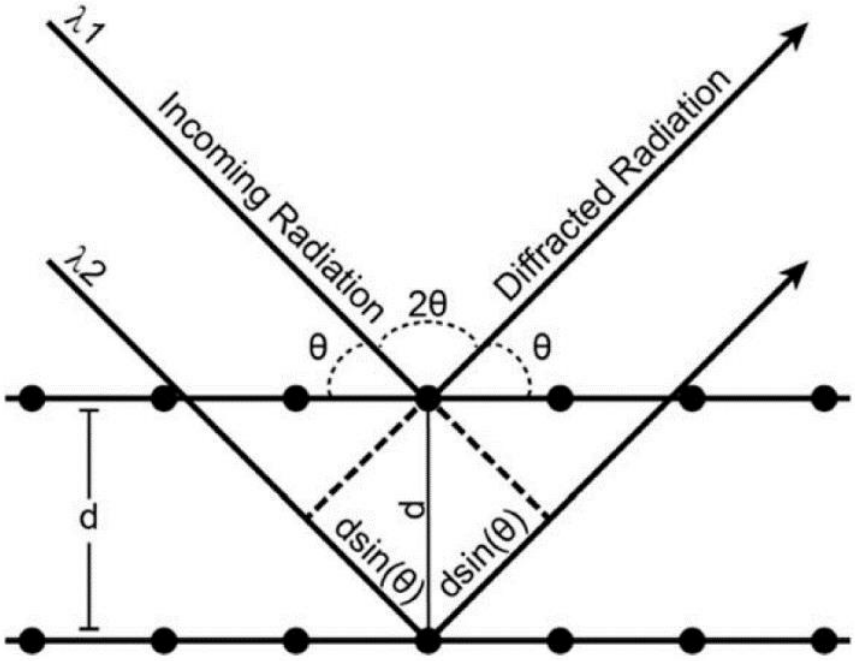

Fig. 3.2 Schematic representation of Bragg's Law conditions [56]

In the current work, the crystalline phases of the nano ferrites were seen in the Materials science Section of the Atomic Energy Center in Dhaka using a Rigaku Smartlab X-ray diffractometer showed in Fig. 3.3. The NMCC ferrite sample was analyzed via X-ray diffraction (XRD) at room temperature, scanning from 15˚ to 80˚ in 0.02˚ increments. The programmable divergence and receiving slits were utilized to regulate the irradiation beam region and the output intensity. The X'Pert High Score software was utilized to analyze the powder diffraction data. With the use of the XRD data, lattice constant values, X-ray densities, an ionic radius, bond length, and hoping length have

been determined. A thorough understanding of the material's structure can be obtained by examining the widths, locations, intensities, and forms of each individual peak. To determine the structural details of the samples, several crystallographic planes have been taken into account. The following relation was used to compute the lattice spacing (interplanar distance), or d, from Bragg's law:

$$2dsin\theta = \lambda$$

$$or, d = \frac{\lambda}{2} sin\theta$$

The following relation has been used to compute the experimental lattice parameter values for each peak,

$$a_{exp} = d_{hkl}\sqrt{(h^2 + k^2 + l^2)}$$

where the crystal plane indices are denoted by the letters h, k, and l.

3.3.2 PHASE IDENTIFICATION

An increasingly useful tool for routine X-ray investigation of ferrite samples is the X-ray diffractometer. The diffractometer technique is also known as the Debye Scherrer technique because of its many inherent benefits. The XRD diffraction lines provide confirmation of the ferrite phase's development. The nanoferrite particles have a cubic shape and a spinel-type ferrite nanoferrite lattice, as indicated by the sharp, well-defined XRD line. Using their peak patterns as a guide, the fcc phase has been seen in every sample.

3.3.3 CRYSTALLITE SIZE ANALYSIS

The Scherrer technique was utilized to ascertain the crystallite size of each nanoferrite sample. The crystallite size has been determined using the samples' XRD pattern of significant peak [311] reflection.

The crystallite size is computed using the formula below:

$$D = \frac{0.9\lambda}{\Delta cos\theta}$$

All crystallite size values for all compositions have been established. All of the samples' crystallite sizes are within the nano range, as confirmed by the XRD spectra's broad spectrum.

Fig. 3.3 RIGAKU SmartLab X-ray Diffractometer

3.3.4 LATTICE PARAMETER

For every sample, the Nelson-Riley approach has yielded the precise lattice parameter of crystalline nanoferrites. Below is the Nelson-Riley function F(θ) [57],

$$F(\theta) = \frac{1}{2}\left[\frac{Cos^2\theta}{sin^2\theta} + \frac{Cos^2\theta}{\theta}\right]^{1/2}$$

All peaks' corresponding values for the exact lattice parameters, a, are plotted along the y-axis, and each sample's F(θ) is plotted along the x-axis. The least-square fit method determines the precise lattice parameter, a_o. This is where the needed precise lattice

parameter (a_o) of the samples is intersected by the fitted straight line on the y-axis. With this approach, at least five crucial reflections are required in order to calculate the lattice parameter. The following formula can be used to get the theoretical lattice parameter,

$$a_{th} = \frac{8}{3\sqrt{3}}\left[(r_A + R_0) + \sqrt{3}(r_B + R_0)\right]$$

where the ionic radii are r_A for tetrahedral and r_B for octahedral.

3.3.5 X-RAY AND BULK DENSITY

We now use the ratio $\rho_x = \frac{8M}{Na^3}$to calculate the X-ray (ρ_x) density. N is Avogadro's number, and M is the ferrite's molecular weight. $P_T(\%) = \left(1 - \frac{\rho_x}{\rho_B}\right) \times 100$ is the formula we use to determine porosity in this scenario [57]. The values of the bulk density ρ_B and the X-ray density ρ_X are used to determine the total porosity, denoted as ρ_T (%) as a percentage.

3.3.6 BOND AND HOPPING LENGTH, IONIC RADIUS

Standley's equation is used to determine the bond length of tetrahedral (A-O) and octahedral (B-O) sites of ferrites from XRD data [58]

$$A - O = \left(u - \frac{1}{4}\right) a\sqrt{3}$$

$$B - O = \left(\frac{5}{8} - u\right) a$$

Here, u represents the oxygen ion parameter, which has the value of $u = \frac{3}{8}$ for the ideal spinel ferrite, and 'a' is the lattice constant.

The ionic radius for tetrahedral (A) and octahedral (B) are, respectively, (r_A) and (r_B).

$$r_A = (A - O) - r(O^{2-})$$

$$r_A = (B - O) - r(O^{2-})$$

Where $r(O^{2-})$ represents the radius of the oxygen ion with a value of 1.35Å.

The distance in magnetic ion, tetrahedral (L_A), and octahedral (L_B) sites are known as Hopping length, which is determined by the formula below,

$$L_A = 0.25a\sqrt{3}$$

$$L_B = 0.25a\sqrt{2}$$

In the case of the determination of porosity, we go through the following equation.

3.4 IMPEDANCE ANALYZER

The dependable Wayne Kerr Technologies 6500B precision impedance analyzer, which is located in the physics department of Chittagong University of Engineering and Technology in Chattogram, is ideal for measuring and analyzing the electric properties of various electronic devices. Apart from that, the 6500B impedance analyzer (Fig. 3.4) is an extremely useful tool for developing circuit designs and for researching and developing materials (both electrical and non-electronic materials).

Fig. 3.4 Impedance Analyzer Wayne Kerr 6500B

3.4.1 DIELECTRIC MEASUREMENT

Pellet-shaped samples were carefully polished to remove any coarseness or surface contamination from other oxides before the experiments were performed. Silver paint was then applied to both sides as a contact material. The complex form depends on the frequency and is expressed as follows [59].

$$\varepsilon^* = \varepsilon' - j\varepsilon'' \qquad (1)$$

Where ε'' denotes the imaginary portion of the dielectric constant and ε' the real portion of the dielectric constant. The ratio of this real and imaginary part dielectric constant ($^{\varepsilon''}/_{\varepsilon'}$) helps to determine dielectric loss tangent ($tan\delta$).

The following relation measures the real part of the dielectric constant ε',

$$\varepsilon' = cd/\varepsilon_0 A \qquad (2)$$

Where A is the cross-sectional area of the flat surface of the pellet sample in cm^2, C is the capacitance in Farad, d is the thickness in cm, and ε_0 is the permittivity of free space [60]

3.4.2 IMPEDANCE ANALYSIS

An extremely important subject to research for the electrical property analysis is impedance measuring. The analysis of electrical qualities and equipment is required. Impedance analysis using ac bridges is used to characterize the prepared samples. The complex impedance of the unknown parameter is provided by the quasi-balance adjustment. The imaginary portion is derived by holding the first variable constant while adjusting the quasi-balance conditions of various elements. The samples that need to have their impedance and standard resistance in sensitive parameters examined are used to create the bridge.

3.4.3 PERMEABILITY ANALYSIS

Four loops of wire are twisted around the ring samples for the electromagnetic investigation. This winding is required in order to reduce undesired capacitance. The coil's turns determine the inductance. Using the following formula, the real part of complicated initial permeability was determined [61],

$$\mu' = \frac{L_s}{L_0}$$

Here, L_0 and L_s represents geometrical inductance of winding coil excluding the sample core and self-inductance value. Using origin software, the initial permeability variation against frequency was plotted. Eddy current has experienced core loss due to the influence of magnetic flux. Remaining loss from the dampening of the reversible domain wall is produced by power dissipation [62]. This also resulted from the reversible rotation of the domains [63].

3.5 PHYSICAL PROPERTY MEASUREMENT SYSTEM

At room temperature, hysteresis loops have been measured using a Quantum Design Physical Property Measurement System (PPMS) housed at the Materials Science branch of the Atomic Energy Center in Dhaka (Fig. 3.5). The PPMS is capable of performing a wide range of physical measurements, including magnetic hysteresis loops, magnetic AC and DC susceptibility, specific heat, thermoelectric figure of merit, and Hall Effect.

Fig. 3.5 PPMS DYNACOOL by Quantum Design

The PPMS gains popularity by applying up to ±10 Tesla within a temperature range of 1.9 - 800 K. The underlying theory behind the PPMS measurement is that when a sample vibrates in closer proximity to a detecting coil, the induced voltage that is already present is measured. With a frequency of 40 Hz, a resolving power of less than 10-6 emu variations of magnetization at a data rate of 1 Hz, and a relatively large oscillation amplitude (1-3 mm peak), a pickup coil is employed in the system. A

vibrator, a coil set, an electronic set to operate the vibrator and track pickup coil changes, and a duplicate of the MultiVu software program for computerization and control make up the PPMS. After the sample rod has been pushed sinusoidally, it must be placed at its end. In the center of a pickup coil, or in its vertical center, is the vibration center. A signal known as an optical linear encoder is obtained from the sample vibrator, which regulates the precise position and amplitude of oscillation. The generated voltage is detected and amplified in the PPMS detecting device. The PPMS detection unit uses the encoder signal as a reference for detection that is currently in place. The PPMS motor unit's encoder signal is used to interpret the raw encoder signal obtained from the vibrator. The PPMS detection device has recognized and averaged the signals obtained from the encoder and pickup coil. The PC application operating the PPMS is then fed this average signal that was obtained.

3.6 ULTRA VIOLET-VISIBLE SPECTROSCOPY

The foundation of ultraviolet-visible spectroscopy is the idea that different spectra are produced when chemical compounds absorb ultraviolet or visible light. PerkinElmer UV-vis Lambda 365 which is situated at Postgraduation lab of Department of Physics, CUET is used to determine optical property.

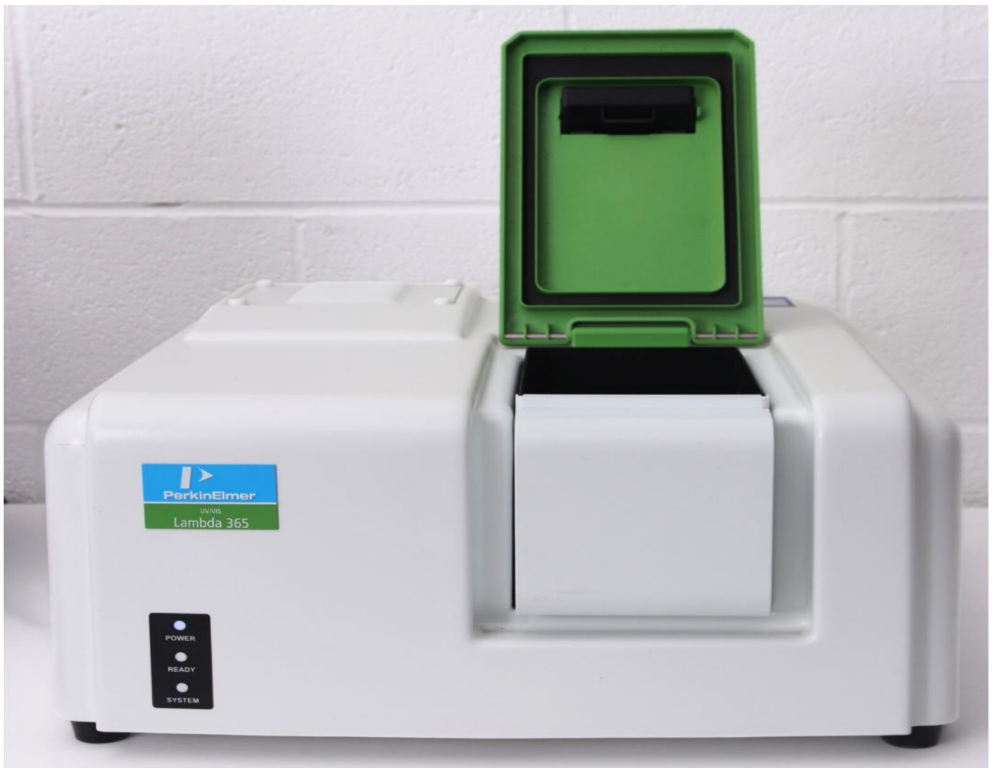

Fig. 3.6 UV-vis Spectrometer Lambda 365

(a)

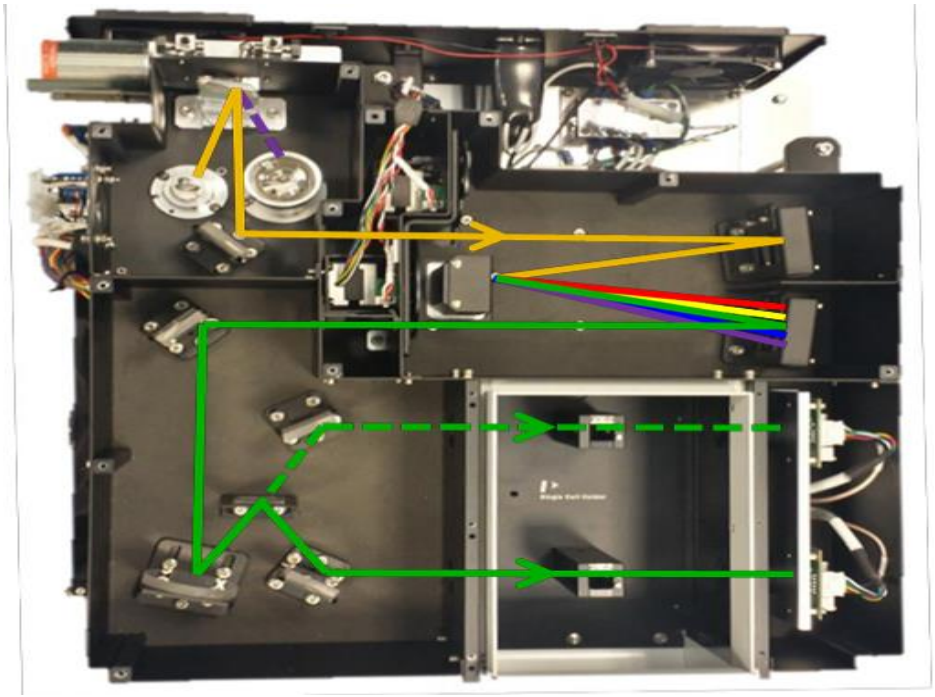

(b)

Fig. 3.7 (a) Lambda 365 optical beam path [64] and (b) reflectance sphere used for powder samples [65].

The light is divided into two beams before it reaches the sample in the Lambda 365 double-beam UV-Vis spectrophotometer. The sample is passed through by one beam,

which serves as the reference. The ratio of the two beam intensities is the measurement that is shown, with 100% Transmission (or 0 Absorbance) serving as the reference beam intensity. The sample and reference beam are measured simultaneously using the Lambda 365 double-beam UV-Visible spectrophotometer, which contains two detectors (photodiodes) (Fig. 3.6). Thick cast plate of Lambda 365 offers unrivalled and robustness in data compared with other pressed metal or plastic design. It also adds to the excellent stability of our data. The lab's thermal effects have no effect on the instrument. Optical path for sample measurement showed in Fig 3.7(a) Reflectance Sphere used to measure the total transmittance or reflectance of solid samples, including paper, metal, glass, fabrics, jewels, and powders depicted in Fig 3.7(b).

The concentration of the sample can be determined directly from the absorption of spectra produced by these samples at specific wavelengths using the Beer Lambert law. The band gap can be determined using this absorbance data which was first stated by Tauc in 1966 [66] Optical absorption depends on the difference between photon energy and band gap, which goes by the following equation, $\alpha h\nu^{1/n} = A(h\nu - E_g)$ [67].

CHAPTER 4

RESULTS AND DISCUSSION

4 GENERAL

This section displays the investigated results and discussed their implications. The results of experiments including XRD, Rietveld refinement, magnetization, dielectric studies, modulus studies, and dynamic conductivity are interpreted in the context of the study's objectives. Each section is covered in detail and properly cited in scholarly literature.

4.1 XRD ANALYSIS

XRD data enables us to investigate the role of Mg substitution in NMCC series. XRD spectra within the 15° and 70° (with searching rate 0.02º) (2θ) NMCC bulk specimen has been shown in Fig. 4.1 sintered at 1423 K. The diffraction peaks (220), (222), (311), (400), (422), (511), and (440) have established a single-phase cubic structure as there are no observed secondary or extra impurity peaks in the limit of measurement. The height and the peak shift varied with the substitution of Mg content and confirmed Mg incorporation in the spinel structure Fig. 4.1. In previous studies, a similar correlation of peak shift corresponding to increasing lattice parameters has also been observed [68]. This variation is because of the incorporation of Mg.

Table 4.1. shows the lattice constant variation concerning the variation of Mg content. The variation in diffraction peaks indicates that the crystallite size of the bulk composition changes with an increasing amount of Mg content, which has been calculated using the Scherrer formula.

Table 4.1. Various parameters determined from XRD data.

Mg^{2+} content y	*Lattice Constant (Å)*			*Volume (Å)*	*Density (ρ)*		*Porosity, P (%)*
	Experimental Lattice Constant	*Theoretical Lattice Constant*	*Rietveld Refinement Lattice constant*		*X-ray Density (ρ_x (gm/cc))*	*Bulk density ρ_B*	
0.0	8.420	8.294	8.424	597.701	5.6	4.89	12.502
0.1	8.423	8.297	8.432	599.447	5.51	5.04	8.600
0.2	8.438	8.312	8.451	603.508	5.41	5.05	6.712
0.3	8.461	8.335	8.467	606.892	5.29	5.03	4.986
0.4	8.440	8.314	8.448	603.016	5.25	4.78	9.014
0.5	8.455	8.329	8.469	607.318	5.15	4.68	9.179

Table 4.2. represents this variation in crystallite size with increasing Mg. Talaat et al. [69] obtained crystallite sizes between 17.4 and 10.2 nm. Sader et al. [70] estimated average crystallite size reduction with the increasing Mg content. This crystallite size is smaller than the experimented one.

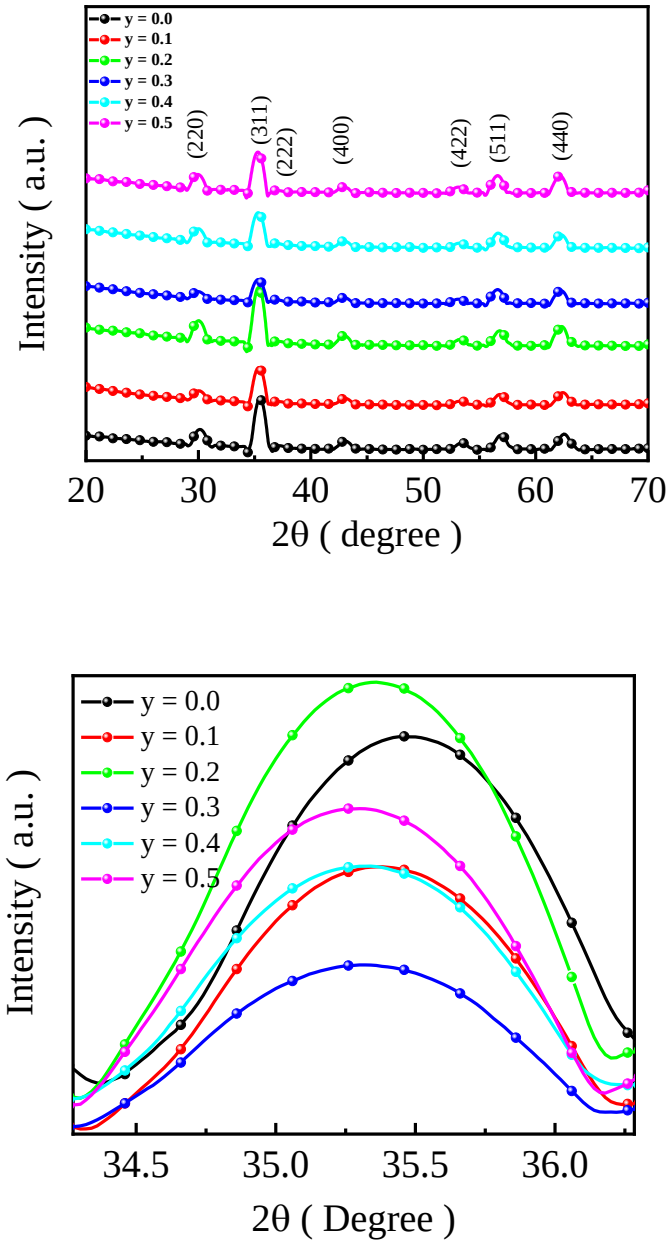

Fig. 4.1 XRD spectrum with prominent peak (311) with visible peak shift.

These characteristics of the following material fulfill the requirement for recording media [71]. The substitution of Mg increases the theoretical and experimental lattice

constants, as mentioned in Table 4.1. The usage of Vegard's Law can explain deviation in lattice constant [72].

Table 4.2. Crystallite size determination for NMCC.

Mg^{2+} content y	*Crystallite size (nm)*			*Lattice Strain*	*Micro Strain*
	Scherer Equation	*Rietveld Refinement*	*Williamson-Hall Plot*		
0.0	69.4	84.6	53.7	0.00586	0.00385
0.1	72.1	89.1	60.6	0.00563	0.00371
0.2	69.7	84.6	53.1	0.00588	0.00385
0.3	64.4	83.9	44.5	0.00630	0.00406
0.4	64.1	83.7	42.3	0.00581	0.00378
0.5	63.7	83.5	41.3	0.00634	0.00410

The substitution of Mg^{2+} shows the decreasing characteristics in density from 5.6 gm/cc to 5.1 gm/cc, which is represented in Table 1.

Table 4.3. Data of ionic radius, bond length, and hopping length for tetrahedral and octahedral site.

Mg^{2+} content y	*Ionic radius (Å)*		*Bond length (Å)*		*Hopping length (Å)*	
	R_A *(Å)*	R_B *(Å)*	*A-O (Å)*	*B-O (Å)*	L_A *(Å)*	L_B *(Å)*
0.0	0.473	0.755	1.823	2.105	3.646	2.977
0.1	0.474	0.756	1.824	2.106	3.648	2.978
0.2	0.477	0.759	1.827	2.110	3.654	2.983
0.3	0.482	0.765	1.832	2.115	3.664	2.992
0.4	0.477	0.761	1.827	2.111	3.655	2.984
0.5	0.481	0.763	1.831	2.114	3.662	2.989

Roy and Bera [73] observed vibrational changes in NiCuZn ferrite synthesized with the combustion technique due to another Mg substitution. As the theoretical density of Mg (1.74 gm/cc) [74], which is way lower than Ni (8.91 gm/cc) [75]. With Mg rising, R_A and R_B ionic radii begin to diverge. Table 4.3. indicates that more divalent Mg has caused changes in the lengths of the tetrahedral (A-O) and octahedral (B-O) bonds. It could be seen as the Mg rises, the hopping length of the (L_A) and (L_B) of magnetic ions showed an uprising trend.

4.1.1 RIETVELD REFINEMENT

The Rietveld Refinement method dedicates the theoretical analysis of crystal structure of substances from experimental XRD data. Fig 4.2. represents the Refinement outcome and illustrates as following: the hollow circles represent the calculated value, and the

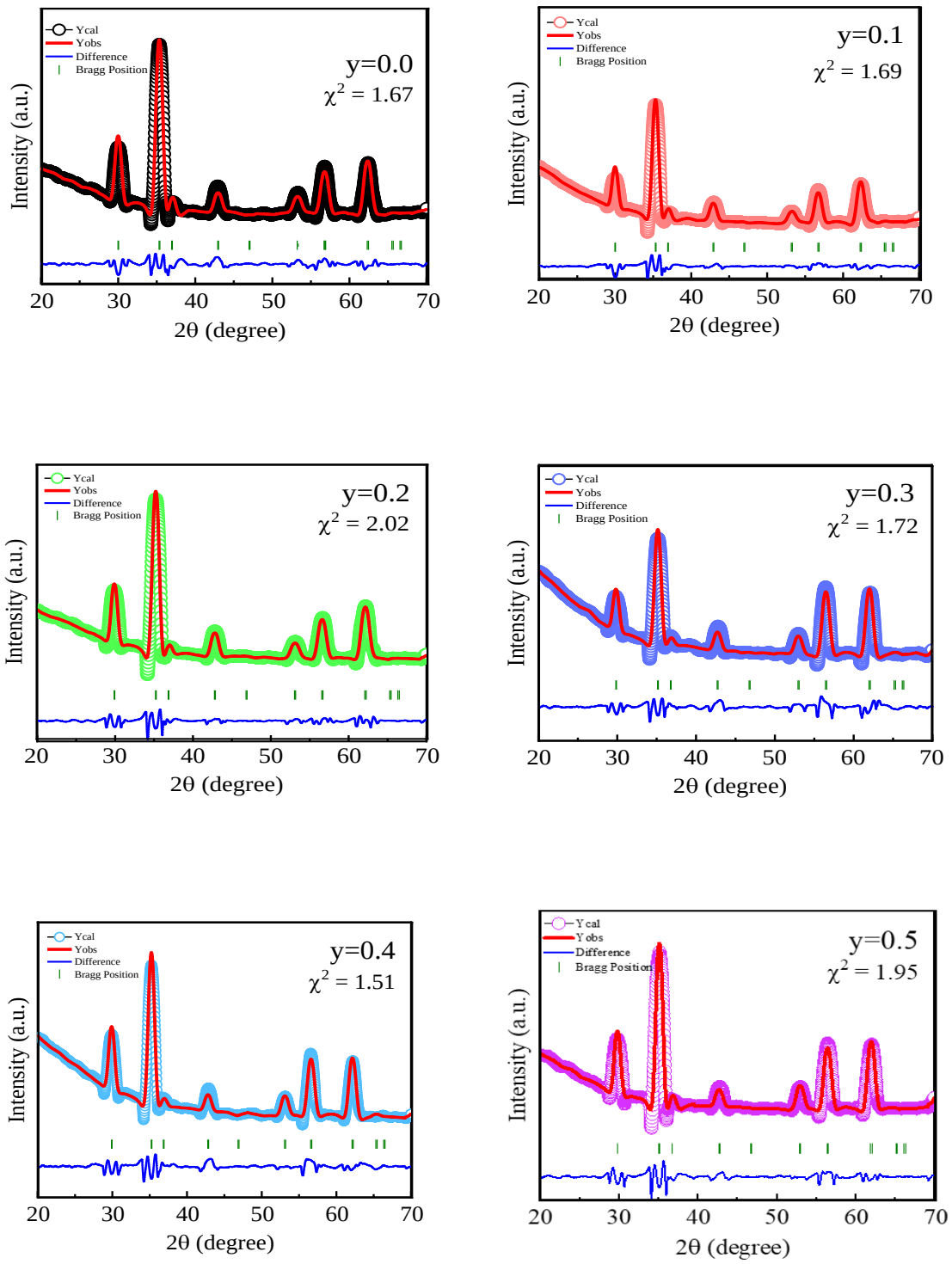

Fig. 4.2 Rietveld Refinement plots for every NMCC samples

red line over the hollow circles represents observed data. A blue line represents the difference between these two data and the dark green parallel line represents the Bragg positions. Rietveld refinement procedure carried numerous times to achieve fitting, thereby obtaining a good χ^2 value [76] and it is less than 4, which is considered as a good-fitting [77]. Within the limit of χ^2 value the corresponding refinement is the procedure for the structural analysis of the face-centered cubic phase of NMCC bulk ceramic.

Table 4.4. Rietveld refinement-fitting parameters for NMCC ferrites.

Mg^{2+} content y	R_p	R_{wp}	R_{exp}	*R factors*		χ^2	*Bragg contributions*	*DW-Stat*
0.0	41.6	16.5	12.8	1.62	2.56	1.67	1.74	0.0141
0.1	41.3	19.4	14.9	1.62	2.85	1.69	1.76	0.0186
0.2	35.8	16.5	11.6	1.36	2.63	2.02	2.11	0.0309
0.3	44.9	21.4	16.1	1.83	3.01	1.72	1.78	0.0183
0.4	40.5	18.3	14.9	1.55	2.54	1.51	1.55	0.0160
0.5	45.4	18.6	13.3	1.57	2.77	1.95	2.03	0.0266

The space group corresponding to this FCC phase is F d $\bar{3}$ m. Other factors like R_p, R_w have been checked, and the quality of the converged fitting, R_{exp}, χ^2 and $DW-stat$ for every composition mentioned in Table 4.4.

4.1.2 CATION DISTRIBUTION

Cation distribution mainly refers to the arrangements of positively charged ions within the crystal structure. In the determination of site preference of crystal, the cationic position is essential. The analysis of cation distribution involves examining the occupancy of the crystal structure and cations using the converged, fitted parameters from the Rietveld refinement [11, 78].

Table 4.5. Cation distribution between tetrahedral and octahedral sites for NMCC ferrites samples.

Mg^{2+} content y	*Cation distribution*	
	A-site	***B-site***
0.0	$(Ni_{0.291}Cu_{0.116}Cd_{0.174}Fe_{0.419})$	$[Ni_{0.210}Cu_{0.084}Cd_{0.126}Fe_{1.580}]O_4$
0.1	$(Ni_{0.236}Mg_{0.057}Cu_{0.118}Cd_{0.174}Fe_{0.415})$	$[Ni_{0.164}Mg_{0.043}Cu_{0.082}Cd_{0.126}Fe_{1.585}]O_4$
0.2	$(Ni_{0.169}Mg_{0.117}Cu_{0.118}Cd_{0.178}Fe_{0.418})$	$[Ni_{0.131}Mg_{0.083}Cu_{0.082}Cd_{0.122}Fe_{1.582}]O_4$
0.3	$(Ni_{0.117}Mg_{0.177}Cu_{0.118}Cd_{0.177}Fe_{0.411})$	$[Ni_{0.083}Mg_{0.123}Cu_{0.082}Cd_{0.123}Fe_{1.589}]O_4$
0.4	$(Ni_{0.053}Mg_{0.210}Cu_{0.106}Cd_{0.158}Fe_{0.473})$	$[Ni_{0.047}Mg_{0.190}Cu_{0.094}Cd_{0.142}Fe_{1.527}]O_4$
0.5	$(Mg_{0.265}Cu_{0.090}Cd_{0.152}Fe_{0.493})$	$[Mg_{0.235}Cu_{0.111}Cd_{0.148}Fe_{1.506}]O_4$

Table 4.5. lists the site occupancies of cations, which have been determined after obtaining good fitting values in Rietveld refinement. From cation distribution, it is clear that Mg^{2+} is preferred in the A-site and shows little contribution in the B-site. Ni^{2+} shows minor variation in occupancy in both sites with the increasing of Mg^{2+}. However, Cu and Cd show their preferences in A-site and B-site throughout the substituted compounds.

4.1.2.1 CRYSTAL STRUCTURE

Using the parameters obtained from Rietveld refinement, such as the unit cell dimensions and angles, one can determine the crystal structure of every composition. Fig 4.3 represents the crystal structures of NMCC for Mg of y = 0.0 to 0.5.

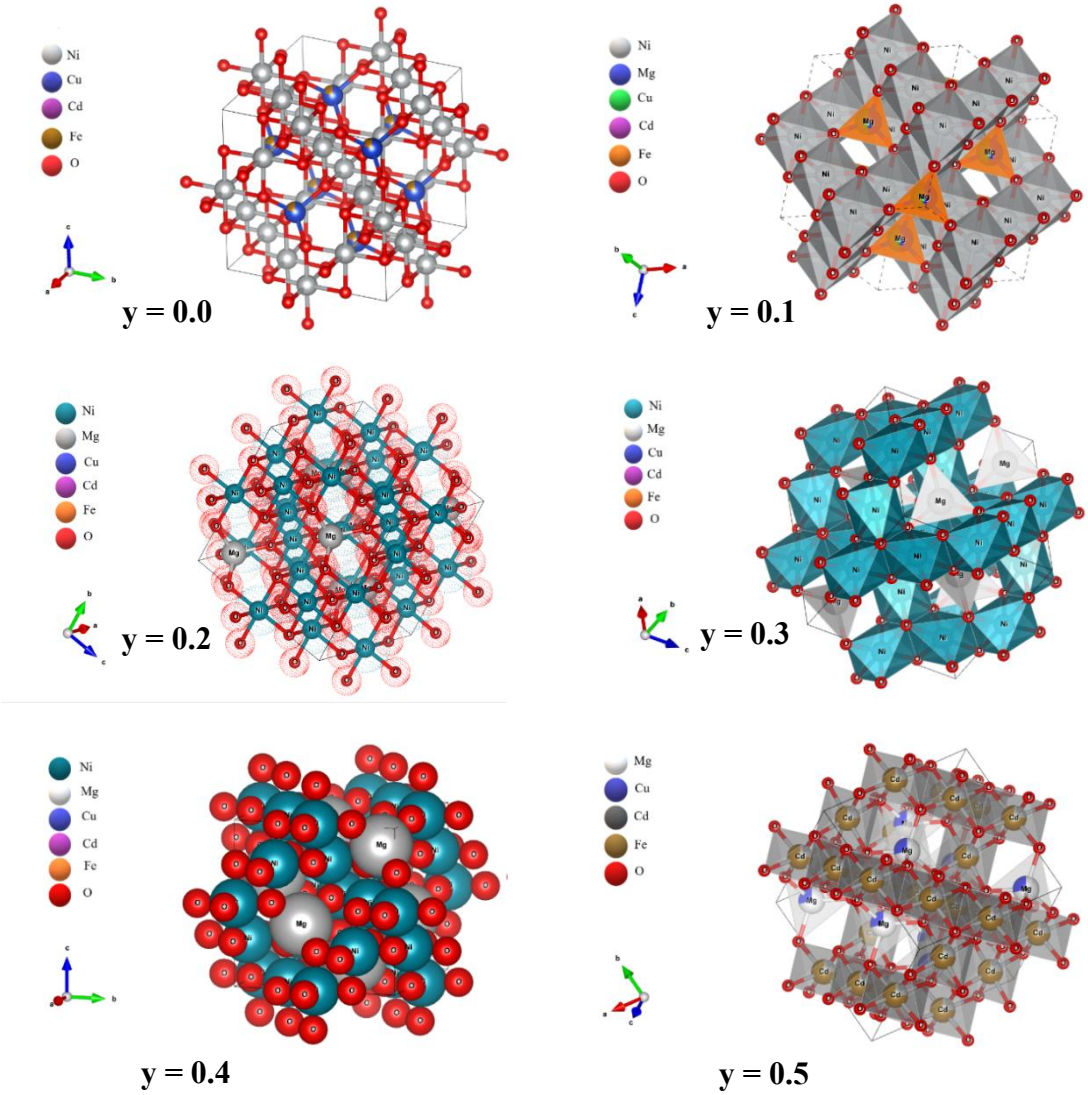

Fig. 4.3 Crystal structure for every NMCC composition.

The crystal structures shown in these figures confirm the formation of FCC crystals. Atoms are illustrated using different colors, and atomic bonds are shown as cylindrical forms. It indicates the polyhedral expression, which exposes the A-site and B-site occupancies of the atoms for cation distribution. It also represents the A-site with grey walls and the B-site with blue walls. Substituted samples of $Mg^{2+,}$ as for y = 0.5, illustrate the similar surrounding phase of sites. A similar kind of crystal representation is seen in previous work [79]. Similar representation for other samples is also done using the same technique.

4.1.3 MAXIMUM ENTROPY METHOD

For electron density determination, researchers used the maximum entropy method (MEM). The calculations for electron density have been initiated using the results of the Rietveld refinement study as the beginning parameters. MEM aims to produce an electron density distribution that meets the observed structural parameters while increasing uncertainty or entropy. This technique gives electron density in the bounding region a clear visualization [80]. Fig 4.4 and 4.5 illustrates the MEM for different compositions using 2D and 3D illustrations. The color variation between yellow and blue represents maximum and minimum charge density respectively. It also indicates few positive and negative values [81]. Similarly, a graphical representation for other samples is done.

Table 4.6. Electron density distribution for various NMCC ferrites samples.

Mg^{2+} content y	***Density***		
	Maximum	***Minimum***	***Sigma Density***
0.0	31.763	-5.001	4.436
0.1	53.579	-9.337	7.477
0.2	70.965	-12.503	9.885
0.3	114.258	-25.654	16.146
0.4	188.938	-33.541	26.261
0.5	20.062	-3.440	2.489

The color pattern legend on the right of each image shows the values of the densities of electrons. The yellow line shows the highest electron densities and the blue line shows the lowest. A few other works have also reported similar imaging patterns [79, 82]. From the MEM, a few values, such as Maximum and Minimum electron density and Sigma density have been evaluated and listed in Table 4.6.

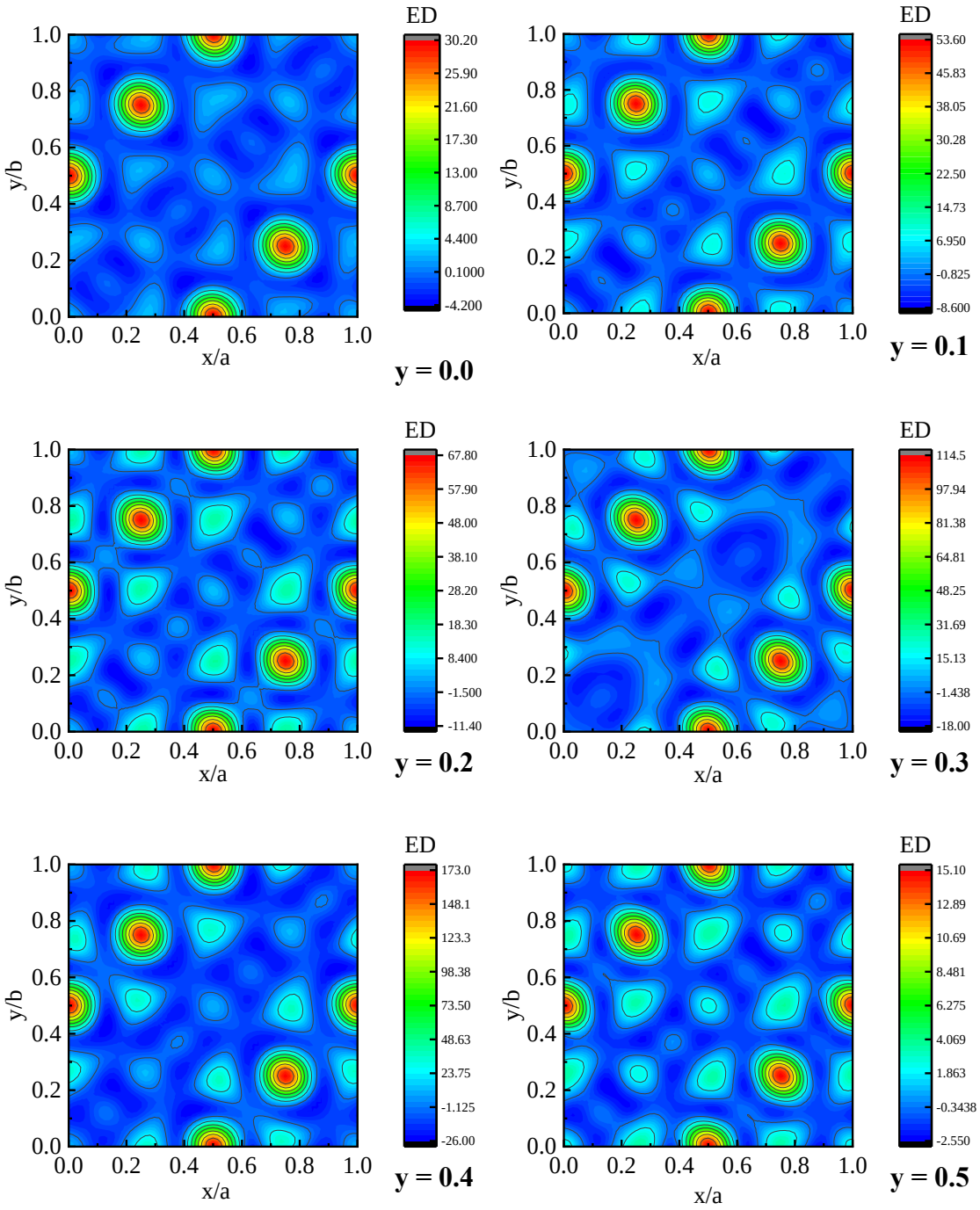

Fig. 4.4 Maximum entropy method plots 2D

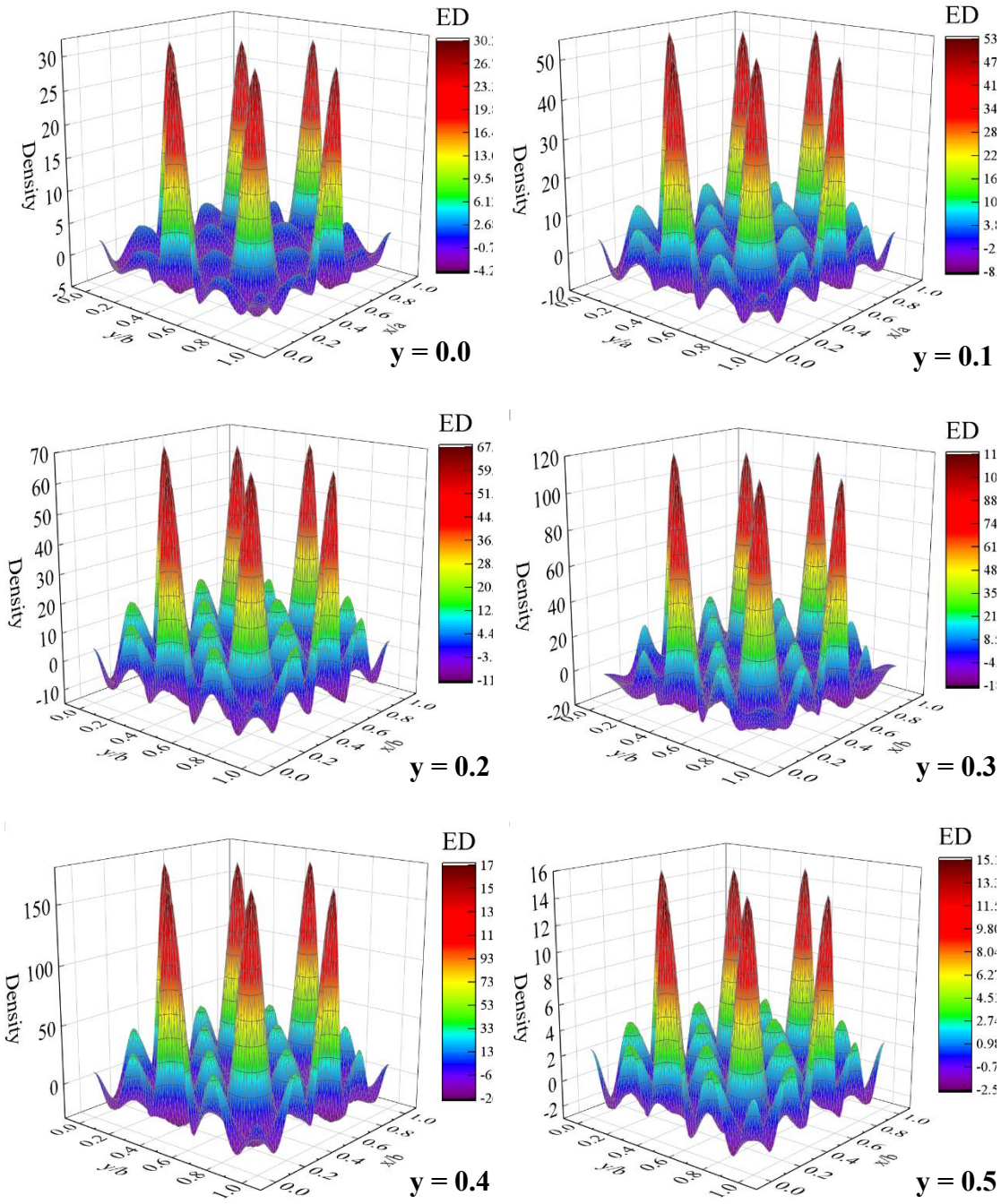

Fig. 4.5 Maximum entropy method plots 3D

4.1.4 WILLIAMSON-HALL PLOT

The Williamson-Hall plot represents the square of the full wave at half maximum (FWHM) of an XRD peak versus the sine of the diffraction angle. The line's slope indicates the inverse of the average grain size, and its y-intercept indicates the lattice micro strain [83]. These peaks could be Gaussian or Voigt-shaped. We used the most

prominent peak (311) for curve fitting of the current series to determine the required Williamson Hall plot.

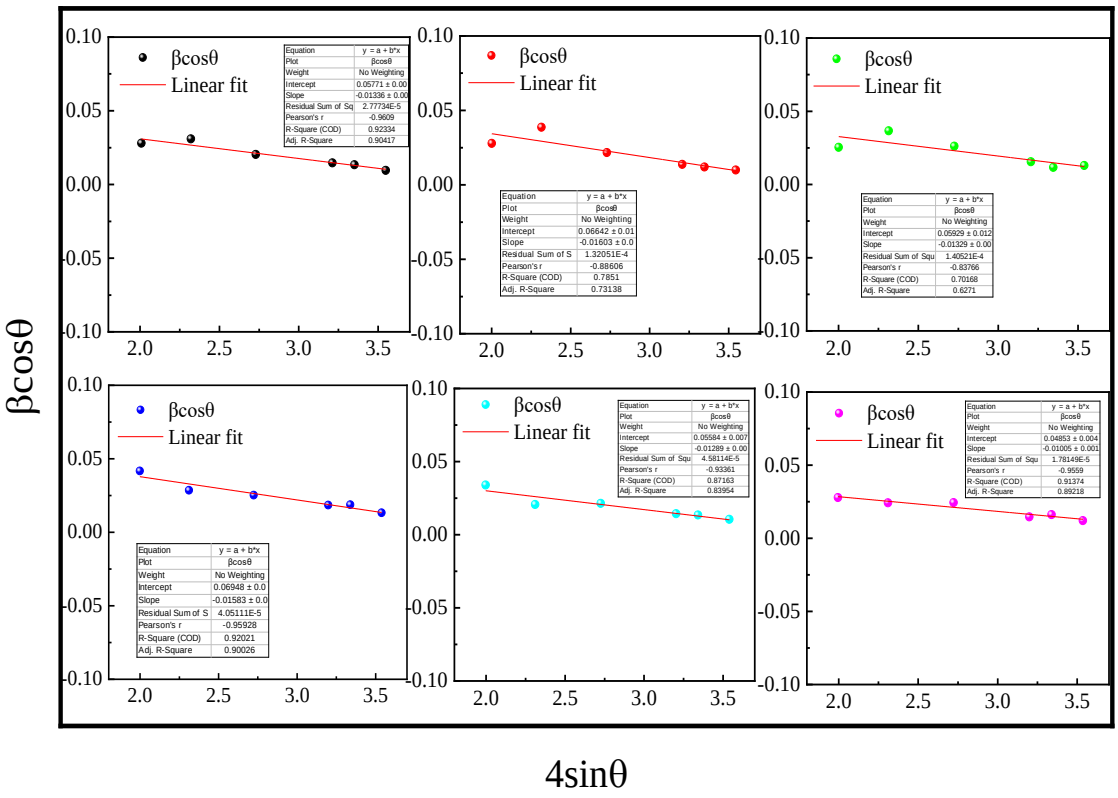

Fig. 4.6 Williamson-Hall plot

It is possible to calculate the crystallite size and microstrain by analyzing the y-intercept and the slope of the line. These drawn W-H plots for all samples are shown in Fig. 4.6, and the changes in crystallite size and microstrain concerning the increasing amount of substitution are presented in Table 4.2. By using Williamson-Hall formula, values for crystallite size and microstrain has been determined. Despite variations in peak values, a slight variation in crystallite size was recorded. For the Mg content, y = 0.1 showed the largest crystallite size of 60.6 nm, and y = 0.5 showed the most diminutive crystallite size of 41.3 nm. All these samples showed negative strains, indicating compression or shrinkage [84]. The positive value of strain is tensile strain, and the negative value is called Compressive strain. They vary in their value of the significant peak shifts. Different peak shifts (Fig. 4.1) were seen in XRD for different substitutions, which shows variation in sizes and represents compressive strains [85].

4.2 DENSIFICATION

The densification of NMCC bulk ferrites from nanopowders has undergone several notable developments. The ρ_X, ρ_B, and P_T for NMCC specimens sintered at 1423 K are given in Table 4.1. and depicted in Fig 4.7. By substituting Mg for Ni in NMCC ferrites, the ρ_B, enhanced as Mg content (y = 0.2) increased. Mg incorporation could have lowered the eutectic temperature of NMCC ferrites [86]. Changes in ρ_B might be the probable cause of P_T in the samples. P_T is the void spaces in the intra or intra-regions of grains of bulk specimens. This P_T of the NMCC specimen is decreased with increasing Mg content [87].

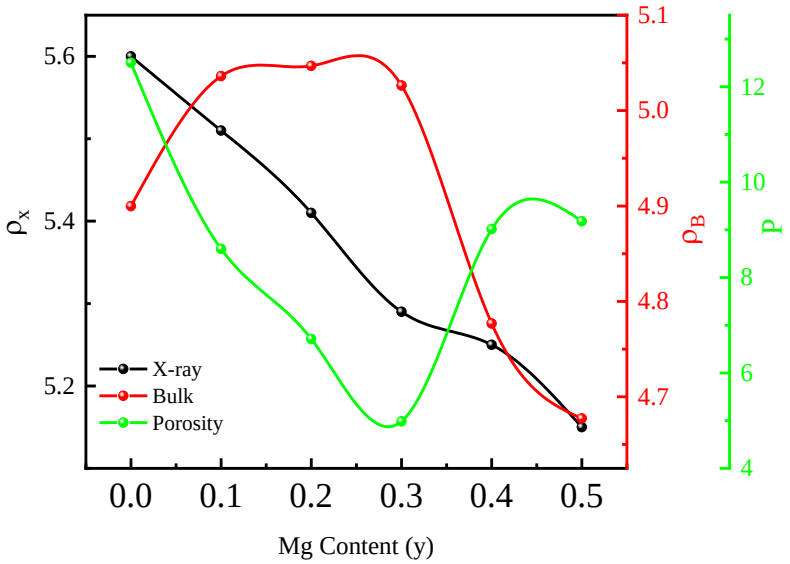

Fig. 4.7 Comparison plot between X-ray and bulk density with porosity

The P_T value decreased significantly from 12.5% to 4.9% between y = 0.0 and y = 0.3 and beyond that showed an increasing tendency for y = 0.4 and y = 0.5. This is because of the difference in the host samples' Ni^{2+} content, which has a density of 8.9 gm/cc, and substituted Mg^{2+} content which has a density of 1.7 gm/cc [88]. This particularly impacts in ρ_B as it could be seen at content y = 0.0 to 0.3, beyond that because of decreasing percentage of ρ_B , the P_T increased to 9.2%.

4.3 SURFACE MORPHOLOGY

SEM provides valuable insights into sample microstructural properties at high magnifications, usually a few times to tens of thousands of times the original size [89]

as shown in Fig 4.8. It is clear from the figure that an increasing amount of Mg substitute in NMCC shows a decreasing tendency in their grain size. The probable cause for this decreasing tendency could be the melting point of Ni (1728 K) which is greater than that of Mg (923 K). Using the ImageJ software, the average grain size (grain diameter) of the samples are determined from electron micrographs [90].

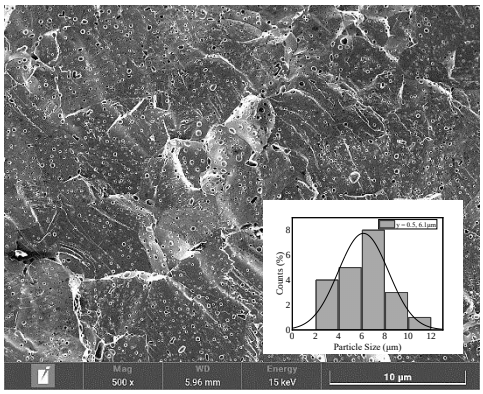

y = 0.0, 6.1 µm

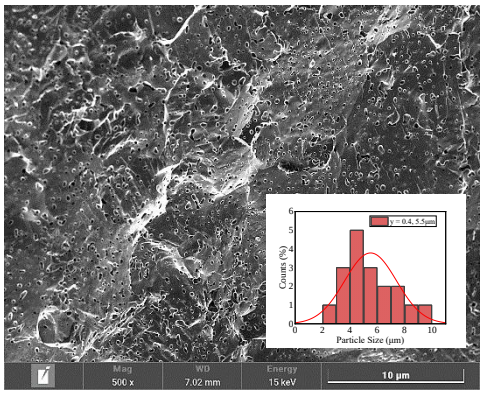

y = 0.1, 5.5 µm

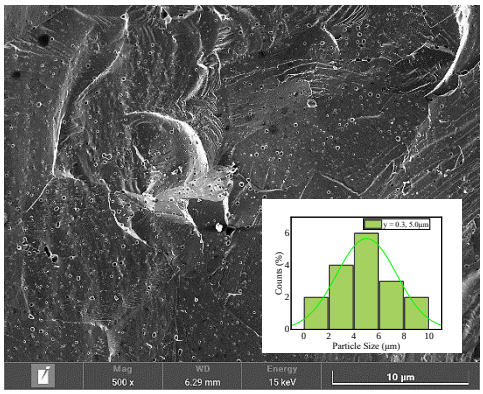

y = 0.2, 5.0 µm

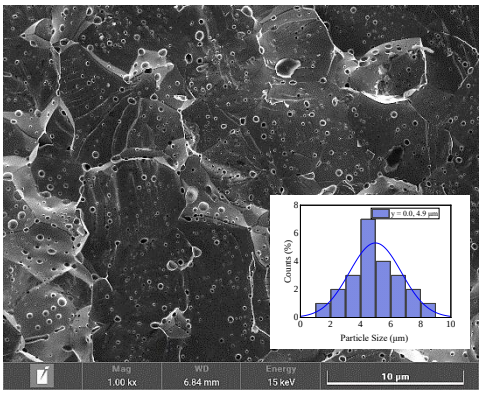

y = 0.3, 4.9 µm

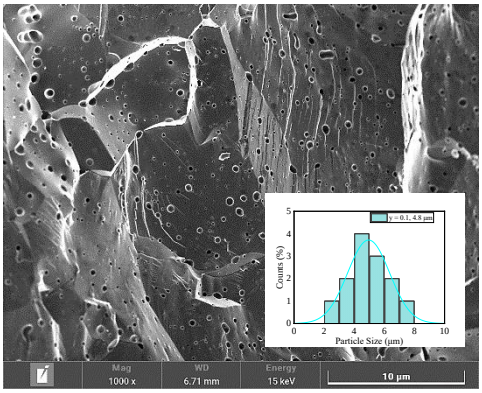

y = 0.4, 4.8 µm

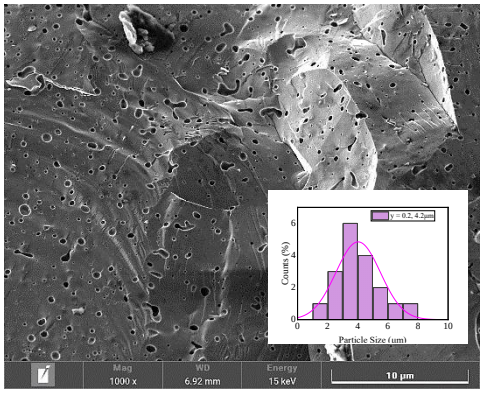

y = 0.5, 4.2 µm

Fig. 4.8 Surface morphology images for every NMCC samples

The grain size has been found in the range of 6.1 µm to 4.2 µm. By analyzing SEM images, nearly uniform is noticed in the sample's grain size. Table 4.1. represents the impact of porosity, which might be the probable corealtion of grain size distribution [91]. According to B.J. Kellett and F.F. Lang [92], this possible grain size variation is related to the densification of ferrite samples. A similar kind of SEM image for Mg substitution is also noticed in previous work [93].

As the snapshot of the SEM image is taken from the interior part of the sample as a result it can be seen that there are pores in the interior portion. Small pores are found in the whole sample along with grain and grain boundaries. That's why it is reasonable that $\rho_{B,}$ is lower than ρ_X.

4.4 OPTICAL PROPERTIES AND BAND GAP

The optical band gap is the energy difference between a material's valence and conduction bands. Here, absorbance data is used to determine this band gap. Absorbance spectra obtained from UV-Vis spectroscopy are depicted in Fig 4.9, covering the wavelength range of 200 nm to 1200 nm. Plotting $(\alpha hv)^{1/n}$ against hv for $n = {}^1/_2$ and $n = 2$ to determine the variation between indirect and direct bandgap. Figures represent each NMCC sample's direct band gap valued between 1.59 to 1.63 eV. Materials that absorb energy in the area of visible light and have colors ranging from red to violet have band gaps between 1.5 eV and below 3.0 eV [94]. To confirm the direct bandgap of NMCC samples within 1.59 to 1.63 eV, Kubelka-Munk function is applied, which goes as, $F(R) = \frac{\alpha}{S} = \frac{(1-R_\infty)^2}{2R_\infty}$ [95]. $F(R)^2$ against hv is depicted in Fig. 4.9 for every composition, which shows the band gap between 1.65 to 1.68 eV. From this, it could be said that NMCC ferrites exhibit semiconducting properties. Fig. 4.10 compares band gap energy between bulk and nanopowder NMCC samples. This comparison shows changes in the bandgap between bulk and nanopowder samples. The band gap determined for powder samples is slightly lower than that of bulk samples. Exhibiting the high value of band gap for bulk samples is considered to be a well-known trait by the quantum confinement effect.

(a)

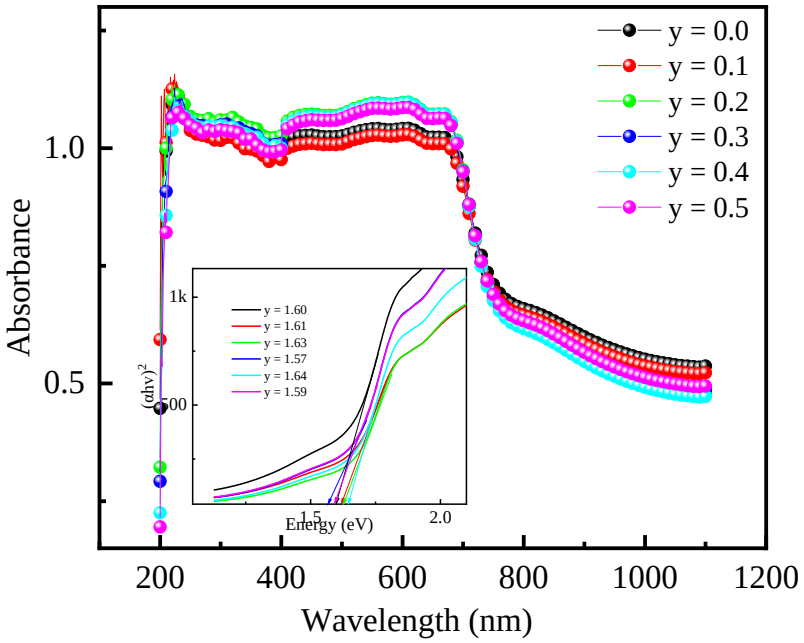

(b)

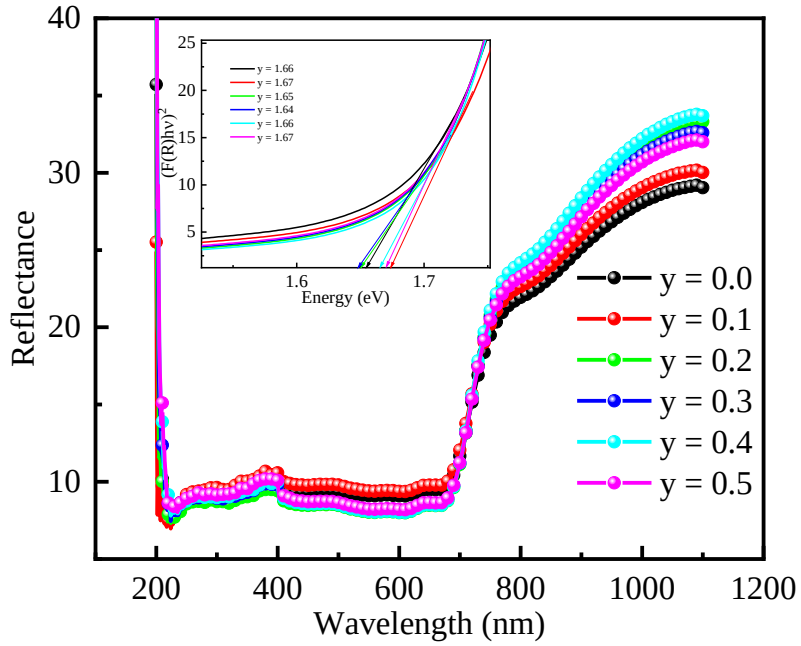

Fig. 4.9 Band gap determination from (a) Tauc method and (b) Kubelka-Munk method

Strong surface interactions between closely packed nanoparticles, an elevated surface-to-volume ratio, and quantum confinement effects due to the very small scale of nanostructured compositions typically cause them to behave differently from the individual bulk components [96].

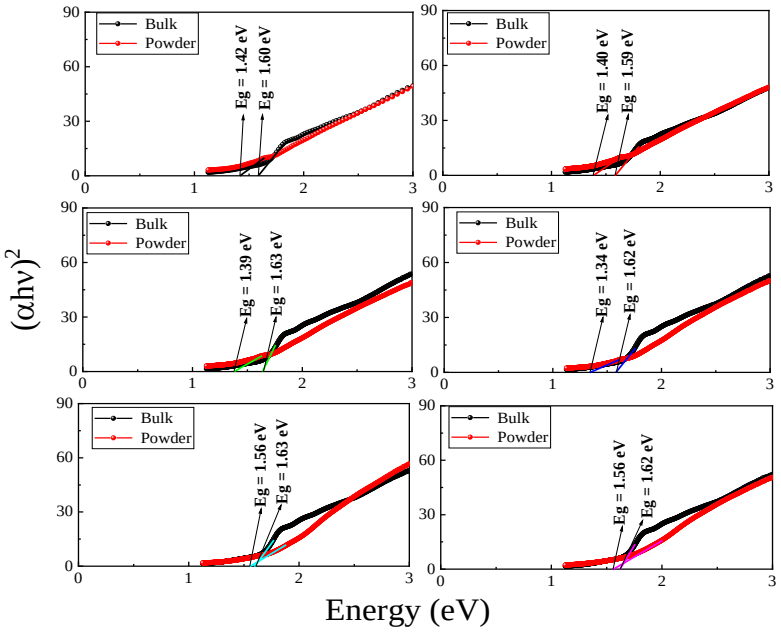

Fig. 4.10 Band gap comparison among Bulk and Nano NMCC samples

4.5 MAGNETIC PROPERTIES

4.5.1 MAGNETIC HYSTERESIS

The magnetic characteristics of NMCC could be due to non-magnetic Mg^{2+} being substituted for Ni^{2+} in spinel superlattice. According to previous work [97], the Mg substitution changes the NMCC coercive field, saturation magnetization (M_s), lattice parameter, and crystallite size.

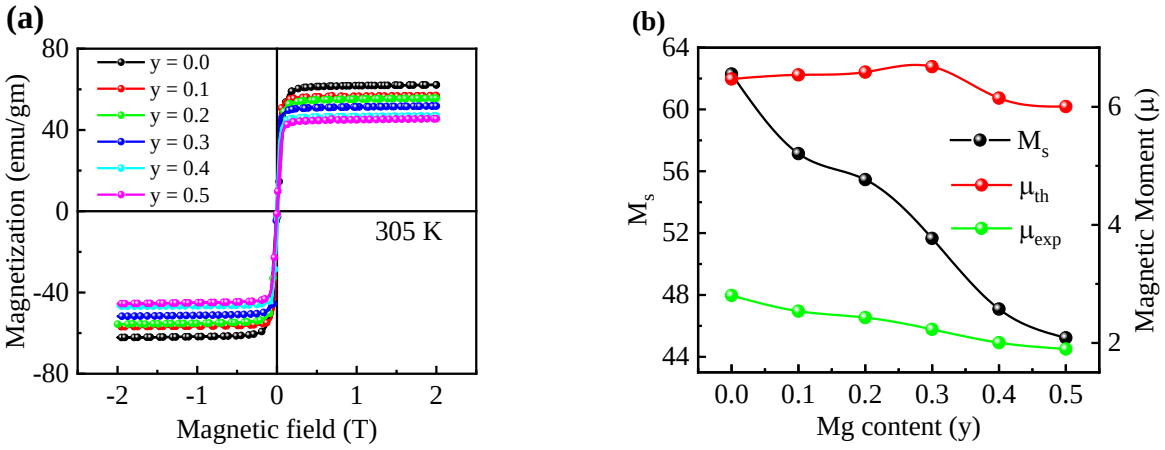

Fig. 4.11 (a) Magnetic hysteresis loop for NMCC and (b) comparison between M_s with theoretical and experimental magnetic moment.

The magnetic hysteresis curve varies with Mg content as depicted in Fig. 4.11 at room temperature. From Fig. 4.11, it is clear that all hysteresis curve is at a ferromagnetic state with low coercivity (H_c), which justifies the soft magnetic nature of the compounds. Various magnetic parameters are also calculated from the magnetization curve, such as M_s, remanent magnetization (M_r), H_c, and remanence ratio (M_r/M_s), which are tabulated in Table 4.7. The M_s decreases with increasing Mg content and shows variation in M_r, H_c, and M_r/M_s. This kind of decreasing M_s is also seen in previous research [98]. The magnetic moment of Mg^{2+} (0.0 μ_B) is less than Ni^{2+} (2.8 μ_B) which might be the probable reason for the decrease in M_s [99].

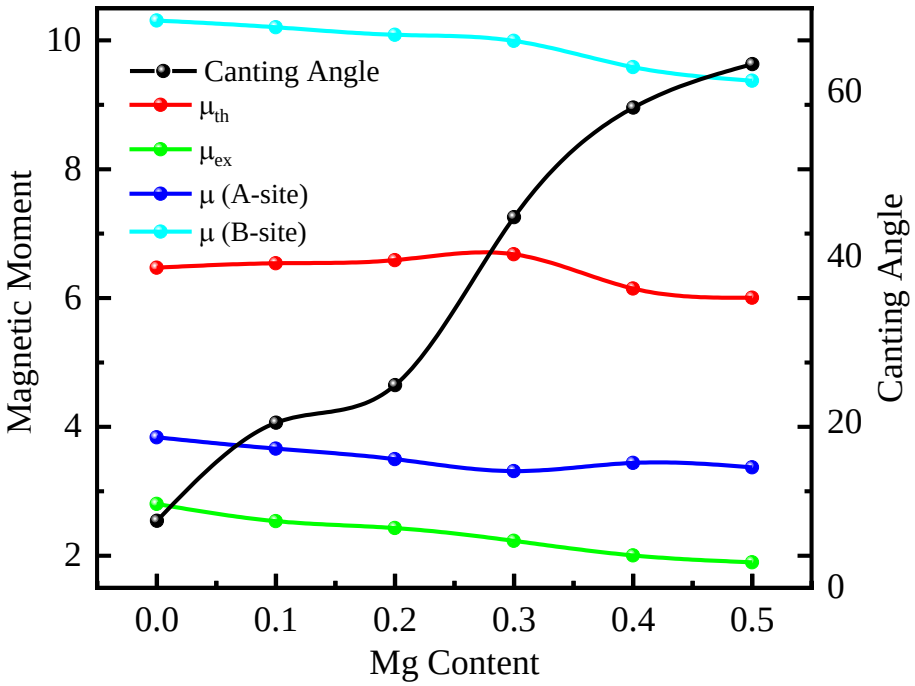

Fig. 4.12 Variation of canting angle with experimental and theoretical magnetic moment.

Cation distribution (Table 4.5) provides a proper interpretation of how M_s is composition-dependent. Mg^{2+} shows a strong preference towards A-site because having a non-magnetic nature [100], whereas Ni^{2+} shows partial preference in both A-site and B-site and Fe^{3+} shows strong preference in B-site and little contribution towards A-site. In this magnetization process, Mg is controlled by site preferences in the spinel structure. Ferrites with spinel structures formed by super exchange interaction could be explained by three exchange interactions: A-B, A-A, and B-B, among which A-B is considered strong interaction. Here AA and BB interaction is ferromagnetic, which is predominated by

antiferromagnetic A-B interaction in defining the magnetic moment of the spinel ferrite compounds. The theoretical magnetic moment (μ_{th}) is the difference between the magnetic moment of B-site and A-site, i.e., $\mu_{th} = \mu_{B(B)} - \mu_{B(A)}$ [101] and experimental $\mu_{ex} = \frac{M_w \times M_s}{5585}$ [102] As Mg increases, M_s decreases as well as μ_{ex} decreases from 2.8 μ_B to 1.9 μ_B. This variation of μ_{ex} and μ_{th} along with cating angle is depicted in Fig 4.12. M_s and anisotropic properties are further analyzed by the law of approach to saturation (LAS) for NMCC bulk and nano ferrites depicted in Fig 4.13 which provides size-dependent magnetic parameters, like M_s, anisotropic constants, etc [103]. Table 4.7. shows the difference between the LAS-fitted M_s for bulk and powder specimens. Here, M_s for bulk are higher than powder specimens.

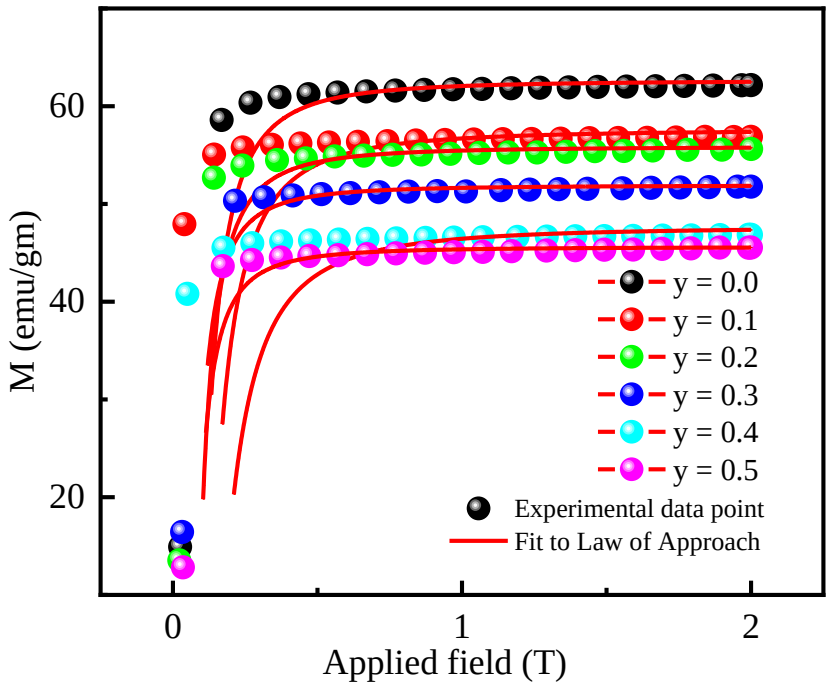

Fig. 4.13 LAS fitted curves for NMCC bulk specimens at room temperature (305 K)

Bulk specimens having many domain orientations, enabling higher M_s value, might cause it. In contrast, nanopowders have fewer orientations with a single domain, which causes rigidity in their domain wall, which reduces the value of M_s.

The anisotropy constant value and coercivity are related, in accordance with Stoner-Wohlfarth theory, by the following relationship: $K_1 = 0.98 \times H_c/M_s$. Here, K_1 is an anisotropic constant that shows variation with changes in H_c value.

4.5.2 TEMPERATURE-DEPENDENT MAGNETIZATION AND CURIE POINT

Curie point (T_c) is the critical temperature where a material loss its magnetic properties and acts as paramagnetic. The magnetic behavior of NMCC ferrites by the step size of y = 0.0 to 0.5 has been observed from room temperature 300 K to 1100 K. This Magnetization and temperature-dependent curve for every specimen is shown in Fig. 4.14.

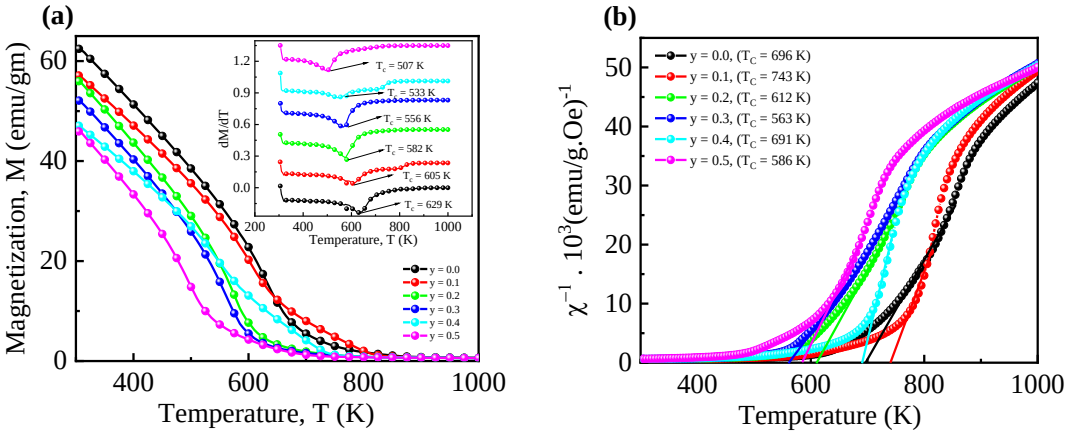

Fig. 4.14 (a) Variation of magnetization with temperature and inset indicates dM/dT as a function of T and (b) inverse susceptibility with T for NMCC ferrites

Using the first point of intersection in the first derivative of the magnetization, the T_c has been calculated, shown in the inset of Fig. 4.14 (a) reduction in T_c can be attributed to the increase in the non-magnetic Mg, which increases lattice parameters as observed in XRD analysis [104]. As the Mg content increases, the variation in the magnetic moment at A and B-sites also caused in weakening A-B exchange interaction results in T_c. Fig 4.14 (b) depicts the variation of inverse susceptibility with the temperature. A clear transitional variation has been seen with the increasing Mg content. A sharp decrease is noticed in T_c from 629 K to 507 K with increasing Mg content. The The following Curie-Weiss law governs the susceptibility in the temperature range, which is significantly above T_c, $\chi^{-1}(T) = {T - \theta_{cw}}/{C}$. Here θ_{cw} is the Curie-Weiss paramagnetic temperature, and C is the Curie constant [105].

4.5.3 MAGNETOCALORIC EFFECT

The determination of the isothermal change in magnetic entropy ($-\Delta S_m$) for all composition through transitions could be achieved using indirect methods [106] for estimation of MCE (magnetocaloric effect) by analyzing the experimental M-T curves

using classical thermodynamic theory and Maxwell's laws [107], $\Delta S_m = \sum_i \frac{M_{i+1}-M_i}{T_{i+1}-T_i} \cdot \Delta H_i$, here experimental values of magnetization are M_i and M_{i+1} measured at T_i and T_{i+1} temperature under the magnetic field H_i (3 T). At T_c, the value of $(-\Delta S_m)$ tends to show the maximum result and varies with increasing amount of Mg, which indicates the change in maximum entropy. It is observed that the magnetic hysteresis influences the magnetocaloric properties of the composition [108].

Table 4.7. Magnetic Hysteresis data of NMCC ferrites.

Parameters	***y = 0.0***	***y = 0.1***	***y = 0.2***	***y = 0.3***	***y = 0.4***	***y = 0.5***
M_s (emu/gm)	62.29	57.14	55.46	51.66	47.09	45.23
M_s by LAS	62.63	57.59	55.85	51.91	47.65	45.61
T_c (K)	630	605	580	555	530	505
RCP(JKg^{-1})	53.82	45.56	46.84	46.08	37.79	38.48
θ_{cw} (K)	741	770	612	586	698	598
H_c (Oe)	31.70	22.40	43.60	42.50	95.00	25.20
M_r (emu/gm)	1.70	3.20	4.20	4.50	9.40	1.90
M_r/M_s	0.03	0.06	0.08	0.09	0.20	0.04
$K_1 \times 10^3$ (Jm^{-3})	2.06	1.34	2.52	2.29	4.66	1.19
$K \times 10^5$ (Jm^{-3})	9.07	7.29	7.05	5.15	25.59	5.44
μ_{th} (μ_B)	6.47	6.54	6.59	6.68	6.15	6.00
μ_{exp} (μ_B)	2.80	2.54	2.43	2.23	2.00	1.90

For ferrites, the variation in the magnetized and demagnetized curve of the hysteresis loop is so insignificant that the heat loss due to hysteresis would be negligible. It has been noted that the curves peaked close to the Curie point, suggesting that when the temperature rises, the ferromagnetic zone gives way to the paramagnetic region. $-\Delta S_m$ found to be shifting towards room temperature with increasing substitution of Mg. It passed 622 K to 486 K at an applied magnetic field of 3T. The changes of $(-\Delta S_m)$ with temperature for each NMCC sample have been shown in Fig 4.15.

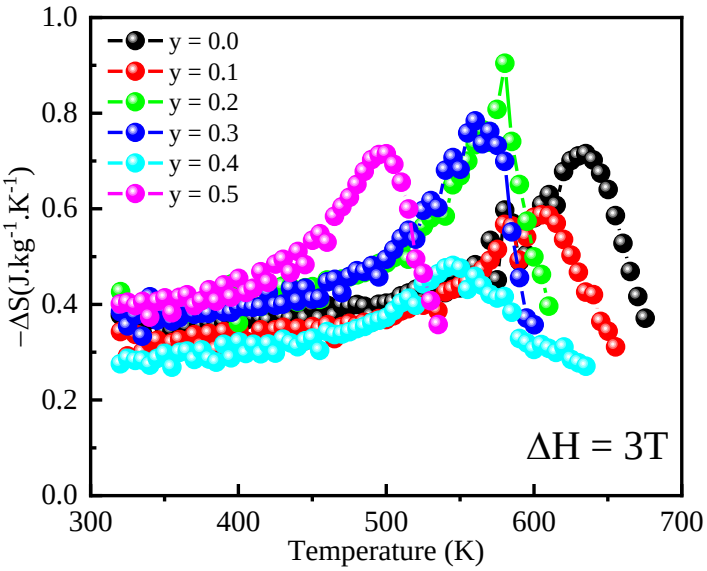

Fig. 4.15 Magnetic entropy variation with temperature at an applied magnetic field of 3 T

Relative cooling power (RCP) is a commonly employed measure for assessing the practical suitability of a material in the context of MCE devices. The value of RCP is the product of FWHM and the maximum value of (-ΔS_m), $RCP = -\Delta S_m \times FWHM$ [109]. This is another significant characteristic of magnetic materials. The quantity of heat transported from the heat source to the cold source during the optimal refrigeration process is measured by the RCP parameter. For the applied magnetic field 3 T, RCP values show a decreasing trend from 53.82 Jkg^{-1} to 37.79 Jkg^{-1} with increasing Mg (Table 4.7). This gives good compatibility for magnetic refrigeration in spite of showing a decreasing trend for all specimens that have high RCP values. All specimens might be employed as a magnetic refrigerant with a broad temperature range of operation, according to the high RCP value have been obtained [110].

4.5.4 INITIAL PERMEABILITY

Magnetic materials have a dynamic feature known as magnetic permeability, also known as permeability spectra in electromagnetism, which allows a magnetic field to arise. Oliver Heaviside first discussed this term in 1885 [111]. Magnetic permeability measures a material's ability to support forming a magnetic field within itself. Fig. 4. (a) represents the μ_i' and 4.23 (b) represents the μ_i''. The expression for the dispersion of frequency in complex initial permeability is as follows, $\mu_i^* = \mu_i' + i\mu_i''$. With

increasing frequency, the behavior of μ_i' generally remains almost constant upto 0.1 MHz frequency. These contributions come from either domain rotation, domain wall displacements, or both [112].

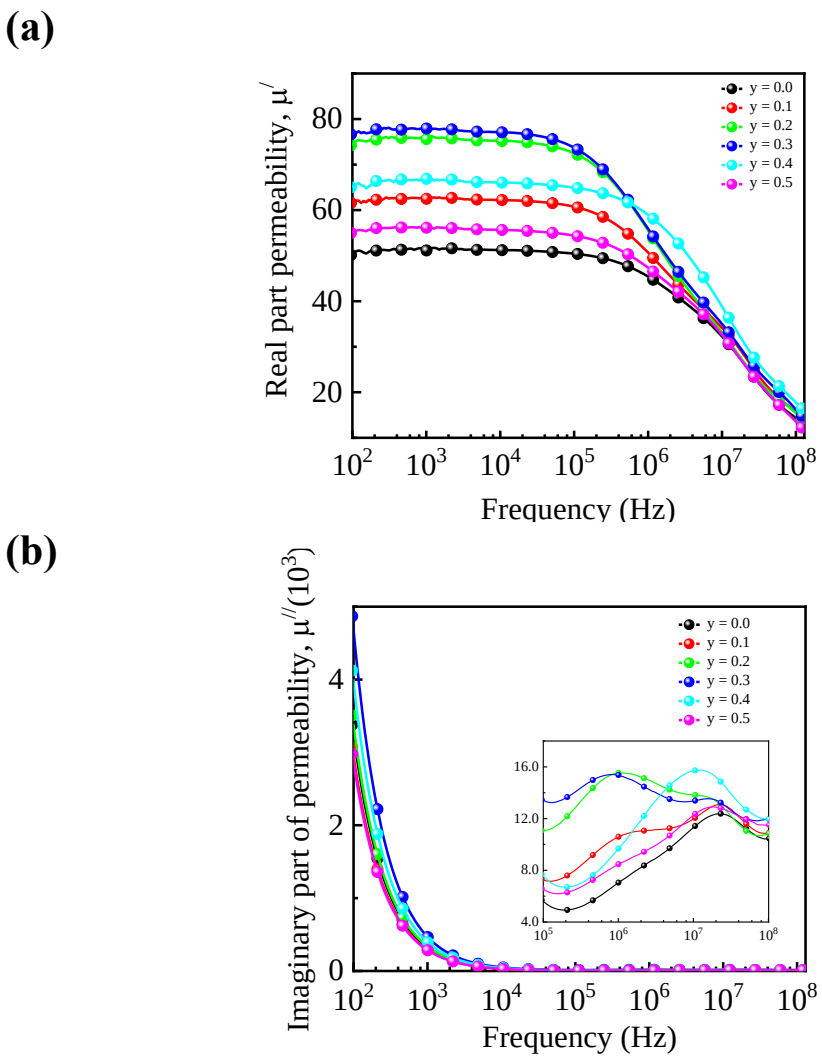

Fig. 4.16 (a) $\mu_i'$and (b) μ_i''variation with frequency for all NMCC ferrite samples.

Analyzing these graphs, the μ_i' of NMCC ferrite samples increased with the increasing amount of Mg content, which its magnetic enhancement also reveals. From Fig. 4.16 (a), the μ_i' variation with increasing frequency reveals linear characteristics at low frequencies at 100 Hz to 100 kHz. This linearity within this region proves its stability with frequency variation. After 100 kHz, permeability falls sharply, which might occur due to approaching cut-off frequency. The permeability of polycrystalline ferrite is affected by two separate magnetization processes, namely, spin rotation and domain wall motion. At lower frequencies, domain wall motion significantly impacts permeability more than spin rotation [113]. The earlier inquiry's show similar behavior [104, 114]. An exception is found, like the μ_i'' plotted in Fig. 4.16 (b). It depicts

decreasing behavior for all samples, and no remarkable changes are seen with increasing frequency. Nevertheless, a peaking nature is seen at a particular frequency above 100 kHz, whereas the μ_i'showed decreasing behavior. The peak shows changes in them with Mg content in the series. These found curves are shown in the inset in Fig. 4.16 (b). The decreasing behavior of the μ_i'' indicates that the $\mu_i'$is entirely responsible for the total contribution of complex initial permeability, which explains the magnetic behavior of every compound.

4.5.5 RELATIVE QUALITY FACTOR

The Relative Quality Factor (RQF) is useful for determining the figure of merit of magnetic material. This RQF is expressed as follows, $RQF = \mu_i/tan\delta$, here $tan\delta$ stands for magnetic loss tangent.

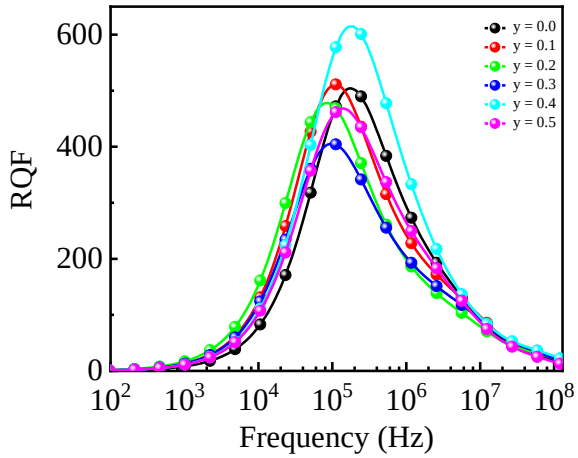

Fig. 4.17 Frequency-dependent RQF curve

Fig. 4.17 shows the RQF variations for NMCC ferrite samples in a range of 20 Hz to 120 MHz frequency. Here, the frequency varies similarly across all samples. The RQF rises with frequency, shows a peaking behavior, and then declines as frequency advances. The peak corresponding to maxima shifts to a lower frequency area as Mg concentration increases. Fig. 4.17 reveals that RQF for Mg^{2+} substituted samples give broader peaks at the intermediate frequency range. At very low and high frequencies, it stays linear. This is due to the intense energy transfer from the applied magnetic field to the lattice at the resonance, accelerating the RQFs lowering [115].

4.6 DIELECTRIC PROPERTIES

4.6.1 COMPLEX DIELECTRIC CONSTANT

The study of dielectric dispersion and electric modulus analysis of NMCC bulk compounds gives valuable information about how much electrical energy stored loss tangent behavior and dynamics of conducting mechanism. The frequency dependent dielectric constant, also known as the relative permittivity are shown in Fig. 4.18 (a) and Fig. 4.18 (b) in the frequency range of 10Hz to 120MHz.

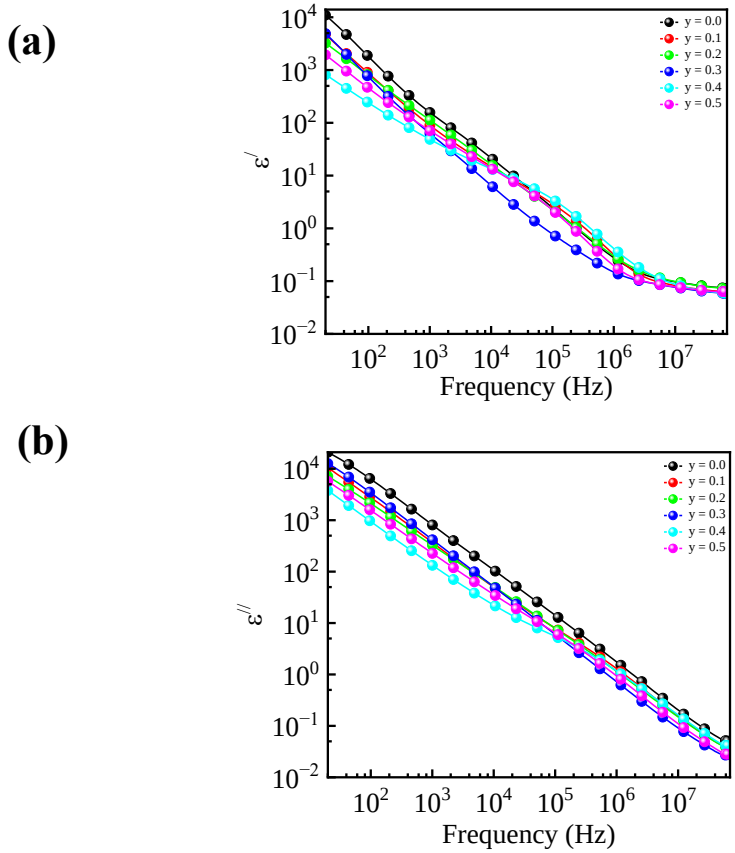

Fig. 4.18 (a) Real part of dielectric constant $\varepsilon^{/}$ and (b) Imaginary part of dielectric constant $\varepsilon^{//}$ variation with frequency of NMCC ferrite samples

Fig. 4.18 (a) the dielectric constant is higher at lower frequencies due to space charge polarization. After 10 MHz, it remains almost constant. Fig. 4.18 (b) similarly represents the imaginary part of the dielectric constant, which shows a usual trend against uprising frequency and shows inversely decreasing in both plots. The dielectric loss decreases with Mg^{2+} concentration. This kind of behavior in accordance of Maxwell Wagner's theory of interfacial polarization can explain space charge polarization and hopping mechanism. Hoping conduction between Fe^{3+} and Fe^{2+} responsible for dielectric losses [116]. Ferrites are well known for having conducting

grains separated by non-conducting grain borders [117]. Hopping allows the electrons to reach the grain boundary, and if the grain boundary's resistance is high enough, the electrons will build up there and cause polarization. With increasing applied field against frequency, the direction of electron motion is reversed frequently. As a result, electrons have fewer chances to cross the grain boundary, which lowers polarization. That is why with applied increasing frequency, the dielectric constant decreases [118].

4.6.2 DIELECTRIC LOSS TANGENT

At room temperature, the dielectric loss tangent ($tan\delta$) is investigated as a function of frequency range 20Hz – 120MHz as shown in Fig. 4.19. A dispersion was detected in dielectric loss tangent plotting with increasing frequency.

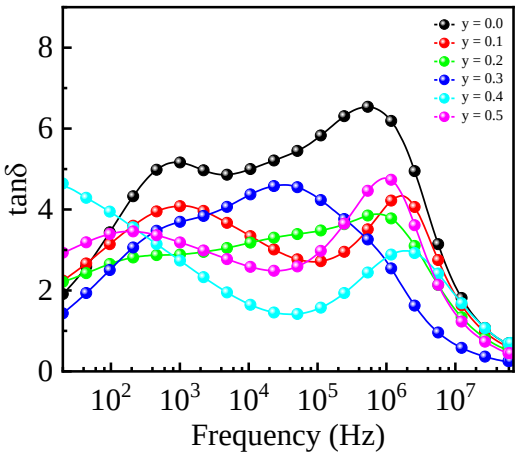

Fig. 4.19 Dielectric loss tangent (tanδ) variation with frequency

The dominant effect of grain boundaries rather than the action of the grains can be used to explain the dielectric dispersion. This is explained by Maxwell-Wagner type interfacial polarization in line with Koop's phenomenological hypothesis [119,120]. The ($tan\delta$) arises from the polarization of its ions, electrons, and dipoles, as well as from its interface. Dipolar and interfacial polarizations control the material's dielectric behavior at low frequencies where ($tan\delta$) arises due to phase lagging of response. At higher frequencies, however, electronic polarization takes over, and the contribution of dipolar polarization diminishes. The phenomenon of dipole relaxation may explain why the ($tan\delta$) falls with frequency [121]. It is that ($tan\delta$) reduces with the increasing amount of Mg in the sites. The loss curve peaks when the hopping frequency of electrons matches the frequency of the applied electric field. The quick rise in electron hopping between nearby octahedral sites at this resonance frequency leads to higher

conduction losses. With additional growth, the $tan\delta$ diminishes and stabilizes with frequency as the frequency of hopping electrons falls behind the frequency of the applied AC field. Because the Mg^{2+} ions escape from the lattice during high-temperature sintering, there are more structural limitations and significant dielectric losses [122]. For the samples utilizing Mg^{2+} as a replacement, two relaxation peaks are discernible. Possible causes of the initial relaxation peak at lower frequencies include the Schottky barrier between the electrode and semiconductor contacts. However, the second relaxation peak is caused by the materials' grains and grain boundaries. Changes in the first peak show the presence of many Schottky barriers with various heights. While the second relaxation peak emphasizes that charge carriers are relaxing at lower frequencies and shows a continuous reduction in the relaxation frequency as the Mg content rises. Because Mg^{2+} substitution reduces charge carrier mobility, samples with larger amounts of Mg^{2+} relax at lower frequencies [123,124].

4.6.3 EVALUATION OF ELECTRICAL MODULUS

The electrical modulus analysis investigates the electrical relaxation mechanism in ion-conducting materials. Due to its benefit of reducing the effects of electrode polarization, modulus formalism is frequently employed to analyze electrical relaxation in ionically and electrically conducting materials [125]. Frequency-dependent real ($M^{/}$) and imaginary ($M^{//}$) parts of electric modulus plotting are depicted in Fig. 4.20 (a) and 4.20 (b).

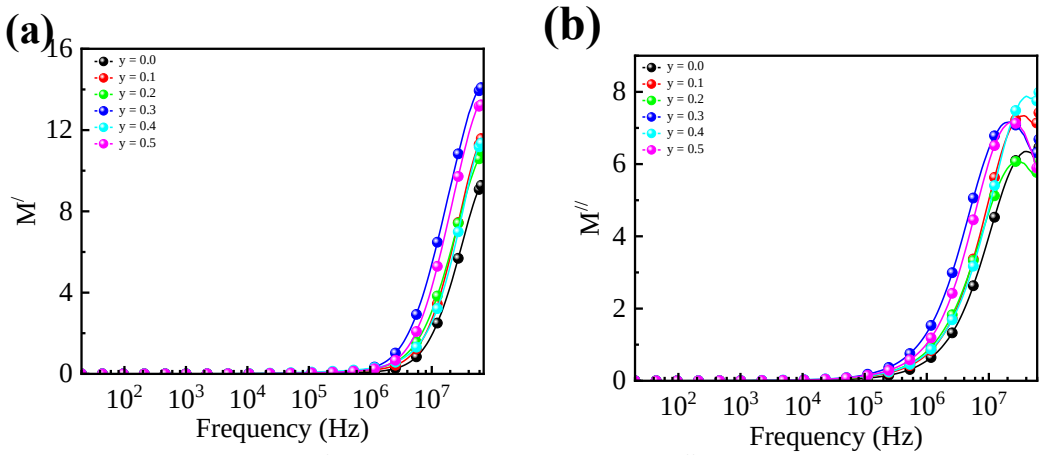

Fig. 4.20 (a) Real part ($M^{/}$) and (b) imaginary part ($M^{//}$) of modulus with frequency variations plot

M′ approaches zero for every substitution amount at low frequencies, and the plot shows conductivity relaxation. Fig. 4.20 (b) represents the M'' also trends similar characteristics to M'. It appears to demonstrate the minimal electrode polarization effects happening at the low-frequency range and in the high frequency range it indicates a release of a space charge polarization. All modulus curve are symmetric, which implies non-Debye relaxation behavior [126]. The Debye relaxation equation links the electric modulus to the Debye relaxation time, which measures how rapidly the polarization relaxes [127].

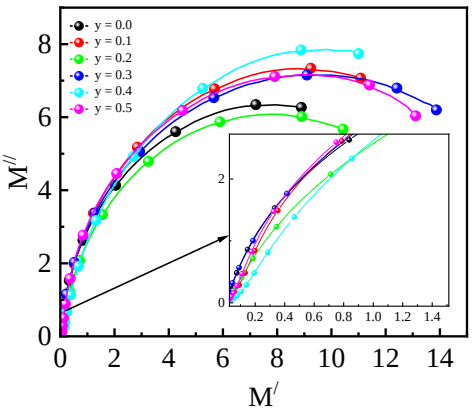

Fig. 4.21 Cole-Cole plot of electric modulus for all NMCC bulk samples

Fig. 4.21 shows the Nyquist plot of the electric modulus for the NMCC series. All substituted samples exhibit a single semi-circular arc, representing that the material is single-phased [103]. This kind of semi-circle originates from the grain contribution [128].

4.6.4 IMPEDANCE SPECTROSCOPY

Fig. 4.22 illustrates the changes in impedance concerning frequency where in Fig. 4.22 (a) it is denoted as a R of the impedance, and the other one Fig. 4.22 (b) explains the X of the impedance. Impedance spectroscopy is essential tool for determining resistance routes, ceramic material structure, and defects. By observing the following Fig. 4.22 (a) and Fig. 4.22 (b), no significant changes are inevitably seen in their plotting. In contrast, only dissimilarity is noticed in Fig. 4.22 (b), which gives a certain peak after 10 MHz frequency. As it is recorded and plotted graph shows that the constant increase in frequency decreases the R continuously.

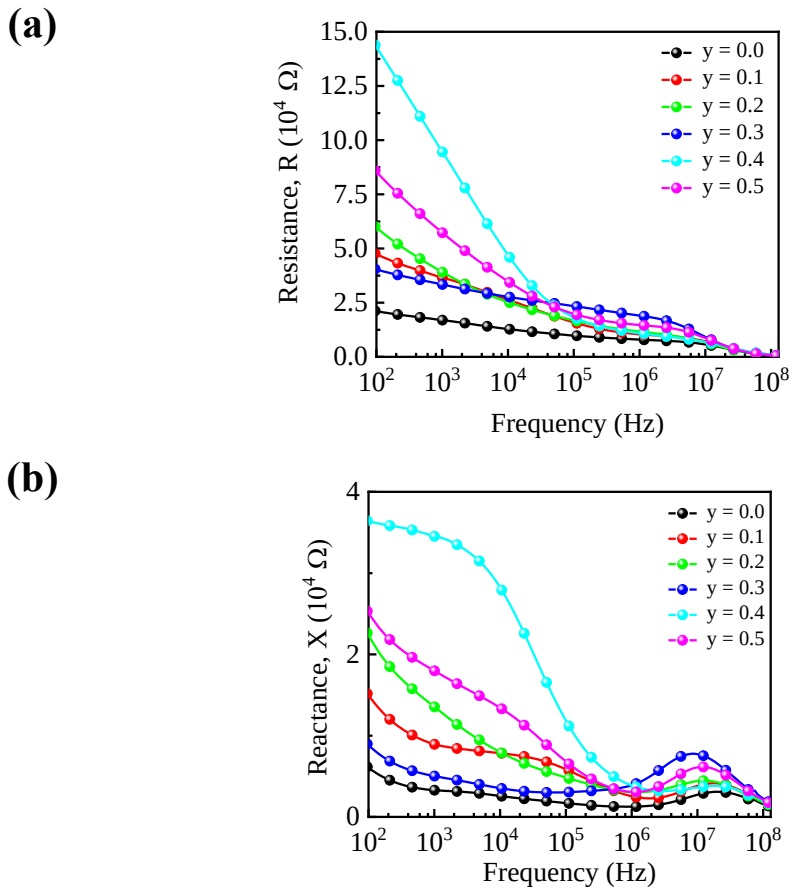

Fig. 4.22 Frequency-dependent NMCC samples variation in (a) R of impedance and (b) X of impedance

Additionally, actual impedance shows an exponential decrease. At the same time, a significant component of the data shows a linear decline. Because of this, it is possible to state that impedance of both types decreases with increasing frequency, which causes a drop in resistance [129].

On the other hand, *X* shows that from 20 Hz to 1 MHz shows growth for Mg^{2+} substitution, and it increases concerning the rising value of frequency. Their impedance variation is almost the same for both R and X. Their value rises from the parent sample at lower frequencies and shows high impedance spectra at low frequencies. On the other hand, in Fig. 4.22 (b), only one semi-circle appeared from all of the samples under study. However, the semi-circle radius of various samples changed by the Mg^{2+} substitution.

4.6.5 COLE-COLE PLOT

The Cole plot with R and X values is shown in Fig. 4.23, depicting the Nyquist plot for Mg substituted NMCC. This plot might be valuable for determining how grain and grain

boundary resistances contribute. The contribution of the grain boundary (R_{gb}) and grain (R_g) resistance is shown in the Cole-Cole plot. From plot, it shows that it has two adjacent semi-circles. The first semi-circle at high frequency describes how R_g contribute, while the second semi-circle at low frequency details how R_{gb} contribute to the conduction process. Due to the electrical contribution and the products' bulk conduction, third semi-circular arcs develop. Fig. 4.24 represents the Cole-Cole plot fitting for a different composition. The distribution of the relaxation time in the material is involved in this sort of impedance spectra behavior. The semi-circular arc separation is a result of the relaxation time constant. Regarding the resistance of R_g, smaller semi-circles are observed in the high-frequency zone, but when it comes to R_{gb}, the semi-circle forms in the low-frequency region. This kind of semi-circular arc is expected for such a compound.

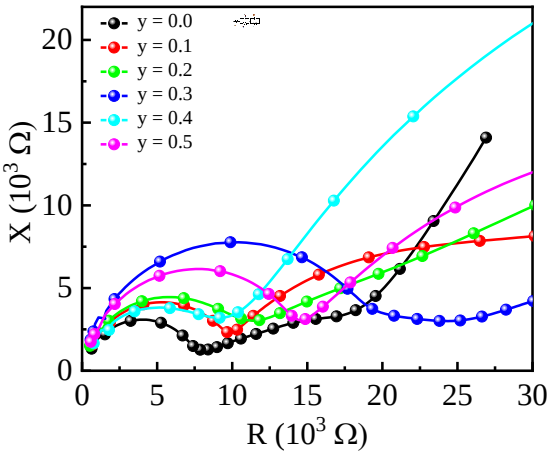

Fig. 4.23 Cole-Cole representation of NMCC samples

R_g, R_{gb}, and electrode effects are equivalent for three consecutive semi-circles. Because of this, the R_{gb} is less than the material R_g. The R_g, R_{gb} and corresponding capacitance (C_g, C_{gb}) have been computed and are presented in the Table. 4.8. This Table reveals the R_g and R_{gb} variation with Mg^{2+} substitution. It is observed that changes in R_g and R_{gb} control the C_g and C_{gb} capacitance. When resistance increases, the value of capacitance decreases, and with the decrease in resistance, it increases the capacitance. Now variation in grain and grain boundary size is also seen in the Nyquist plots in some compositions at low frequencies, giving significant grain contribution and larger grain boundary diameter.

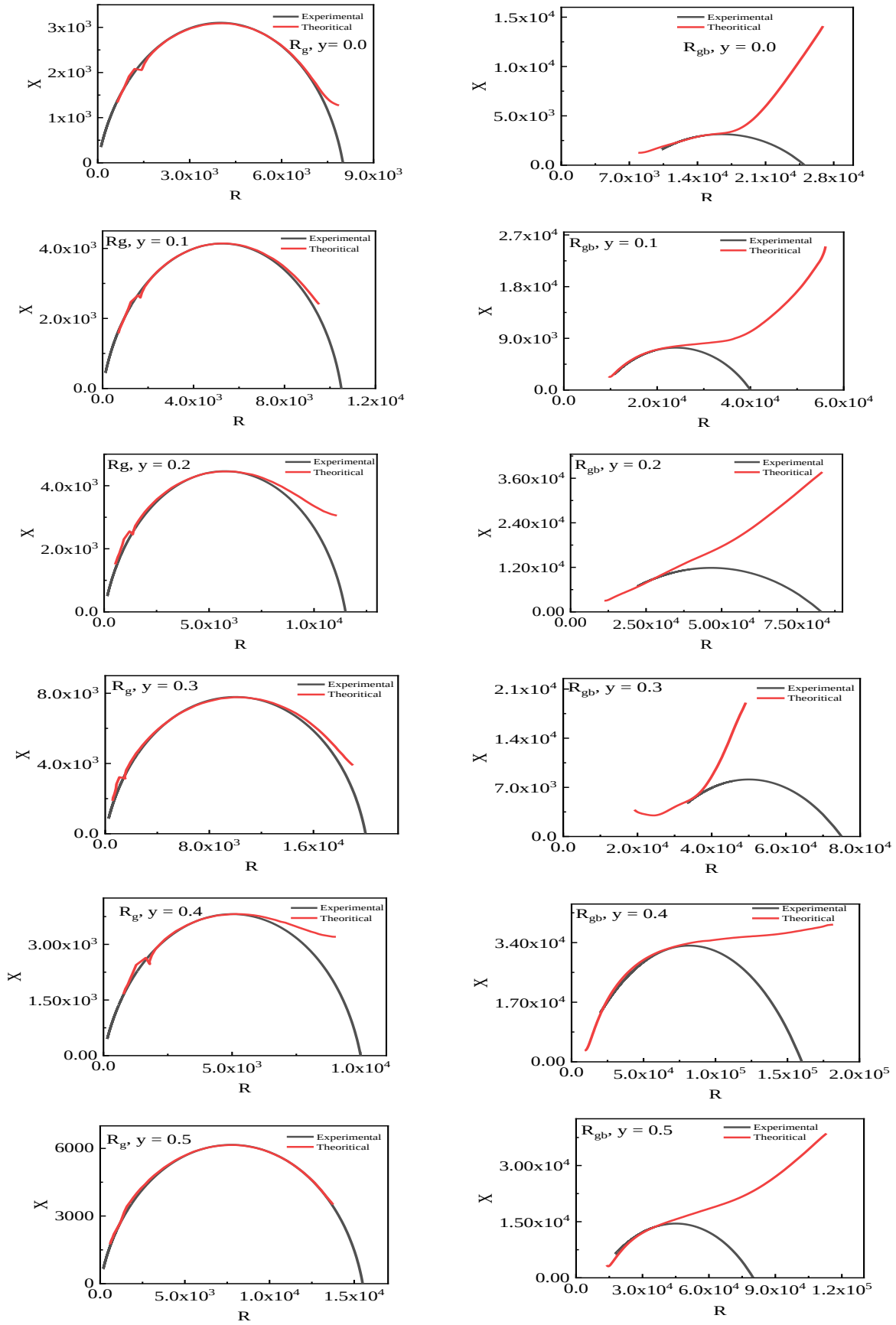

Fig. 4.24 Theoretical fitting for grain and grain boundary resistance.

The opposite nature is also seen in grain boundaries, like small grain arcs and large diameters. Imperfections at the grain boundary site regulate the type of transport, increasing the grain boundary's contribution to the overall resistance. Therefore, it is anticipated that grains will contribute to the impedance of inter-grain zones and have a lower concentration than grain boundaries [114].

Table 4.8 Grain and grain boundary parameters for various NMCC ferrites samples.

y content	R_g (kΩ)	R_{gb} (kΩ)	C_g (μF)	C_{gb} (μF)
0.0	8	17	0.074	0.83
0.1	10.5	32	0.070	0.49
0.2	11.5	73	0.023	0.31
0.3	20	50	0.009	0.42
0.4	10	15.7	0.072	0.84
0.5	15.5	70	0.017	0.36

4.6.6 Ac CONDUCTIVITY

In Fig. 4.25, at the frequency range of 20 Hz to 120 MHz, the conductivity of NMCC bulk sample has assessed at room temperature. Conductivity increases slowly at lower frequencies but quickly at higher frequencies. Low conductivity values are seen because of the contribution of insulating nature of grain boundaries' variation at lower frequencies. Low frequency results due to low AC conductivity and low electron hopping between Fe^{2+} and Fe^{3+} at octahedral sites [130]. Higher frequencies make grains with high conductivity more active, which increases the hopping of the charge carrier between the ions as a result improve conductivity [131]. Jonscher's power law [132], establishes a relationship between frequency-dependent and frequency-independent ac conductivity, which is expressed by the following equation, $\sigma(\omega) = \sigma_{dc} + A\omega^n$. Where n is the frequency exponent with $0 < n < 1$ and A is the temperature dependent pre-exponential component. All dispersion phenomena are

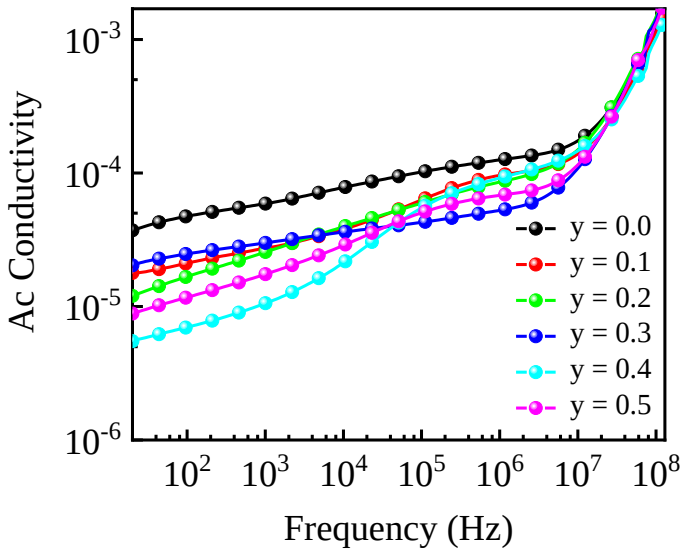

Fig. 4.25 Ac conductivity curve against frequency for all NMCC samples

characterized by the term $A\omega^n$, which includes the ac dependency. The conductivity value steadily declines as Mg concentration rises, and the NMCC y = 0.4 sample has the lowest conductivity value among all the sample. Higher frequency results in faster dipole responses to changing fields, which increases conductivity. The hopping conduction of charge carrier might be the probable reason for rise in conductivity as charge carrier motion decreases the resistance and increase conductivity [113].

CHAPTER 5

CONCLUSIONS

Chapter 5: CONCLUSIONS

5.1 GENERAL

In this study, the effects of Mg substitution on the structural with Rietveld analysis, magnetic with magnetocaloric effect, dielectric, and electric properties of dense Ni-Cu-Cd bulk ceramics detained from nanocrystalline powder successfully and analyzed using the dense specimen.

5.2 KEY FINDINGS

The acquired results could be used to mention the following important conclusions;

- $Ni_{0.5-y}Mg_yCu_{0.2}Cd_{0.3}Fe_2O_4$ single phase bulk specimen obtained from sol-gel synthesized nanopowders sintered at 1423 K temperature.
- Both XRD and Rietveld refinement show decreasing of lattice constant with Mg content obtained goodness of fitting value (χ^2= 1-2) as well as structural parameters like lattice parameters, single phase structures justify space group, etc. matched well with the experimental (XRD) values.
- Cation distribution reveals Mg substitution in NMCC compositions show occupy on both A and B sites though slightly larger in the tendency towards A-sites.
- The electron density distribution shows both the covalent and ionic bond occupancy increased with Mg, content up to y = 0.4.
- Surface morphology study it is revealed that grain size decreases with Mg for its having lower melting point and porosity decreased remarkably up to y = 0.3 beyond it increases where intergranular pore size becomes larger.
- The optical bandgap of NMCC has been investigated and showed an increasing tendency with Mg. They could be classified as good candidates for visible light absorption. Compared to nano powders band gap in bulk specimens shows an increasing trend.
- Magnetic saturation shows a reduction with increasing Mg content. LAS fitting shows a similar tendency as the experimental value.
- At Curie temperature (Tc), temperature-dependent magnetic data exhibit an abrupt transition from ferrimagnetic to paramagnetic.
- All of the samples' measured magnetic entropy changes showed a maximum at their respective Tc and increased with Mg content, as shown by the M-T curve

calculation of magnetic entropy, which likewise decreased with Mg content due to the reduction of exchange interaction as seen in canting angle. Relative Cooling Power ratings of the magnetic field specimens at 3 T are high, suggesting that they could be good candidates for magnetic refrigeration.

- Dielectric loss tangent has been reduced remarkably by the Mg substitution.
- Real part of the electric modulus has saturated at high frequency and the imaginary part of the electric modulus shows peaking behavior due to transition between long range hopping to short range hopping.
- Contribution of grain and grain boundary resistance has seen from the Cole-Cole plot and theoretical fitting to calculate the quantitive values.
- Ac conductivity reduction with Mg content reduces at high frequency which would be the main component as MLCI.

LIMITATION OF THE STUDY

Due to lack of proper availability of characterization facility of various instruments like XRD, FESEM, PPMS etc. practical handling was limited during research time.

PRACTICAL IMPLICATION

The result has found potential for Magnetic Refrigeration as it provided great value of Relative Cooling Power.

RECOMMENDATION FOR FURTHER STUDY

Temperature Dependent magnetization needs to be done on various magnetic field (i.e. 1T to 5T) to obtain optimum for RCP values and to get certainty on being applicable as Magnetic refrigerant. Also, FTIR, P-E hysteresis loop and analysis is required to obtain clear image of this research.

BIBLIOGRAPHY

[1] S. S. Ata-Allah, M. K. Fayek, H. A. Sayed, and M. Yehia, Mater. Chem. Phys. **92**, (2005) 278.

[2] A. K. M. Akther Hossain, T. S. Biswas, T. Yanagida, H. Tanaka, H. Tabata, and T. Kawai, Mater. Chem. Phys. **120**, (2010) 461.

[3] M. M. Hossen and M. B. Hossen, J. Mater. Sci.: Mater. Electron **30**, (2019) 20801.

[4] H. Su, X. Tang, H. Zhang, L. Jia, and Z. Zhong, J. Magn. Magn. Mater. **322**, (2010) 1779.

[5] P. K. Roy and J. Bera, J. Magn. Magn. Mater. **298**, (2006) 38.

[6] D. M. Liu, J. Mater. Sci. **29,** (1994) 1507.

[7] X. Qi, J. Zhou, Z. Yue, Z. Gui, and L. Li, Magn. Magn. Mater. **251,** (2002) 316.

[8] Y. Tajima, Z. Nagasawa, I. Tanabe, H. Yamada, K. Kusaba, and J. Tadano, Microbiol Immunol **36,** (1992) 1233.

[9] R. Breitwieser, U. Acevedo, S. Ammar, and R. Valenzuela, AIP Adv. **7,** (2017) 055813

[10] P. K. Roy and J. Bera, Mater. Chem. Phys. **132**, (2012) 354.

[11] S. M. Kabbur, U. R. Ghodake, R. C. Kambale, S. D. Sartale, L. P. Chikhale, and S. S. Suryavanshi, J. Electron. Mater. **46**, (2017) 5693.

[12] P. Chavan, L. R. Naik, P. B. Belavi, G. Chavan, C. K. Ramesha, and R. K. Kotnala, J. Electron. Mater. **46**, (2017) 188.

[13] R. Valenzuela, T. Gaudisson, and S. Ammar, J. Magn. Magn. Mater. **400**, (2016) 311.

[14]. W. H. Bragg, Lond. Edinb. Phil. Mag. **30,** (1915) 305.

[15] C. A. Bates, M. J. Oglesbyss, K. J. Standleys, J. Phys. C: Solid State Phys. **5,** (1972) 2949.

[16] M. J. Iqbal, M.R. Siddiquah, J. Alloys. Compd. **453,** (2008) 513.

[17] G. W. Stinton, J. S. O. J. Appl. Crystallogr. **40,** (2007) 87.

[18] K. Shankland, J. Res. Natl. Inst. Stand. Technol. **109,** (2004) 143.

[19] D. J. Craik, Magnetic Oxides, **798,** (1975) 175.

[20] A. Bagum, M. B. Hossen, F. U. Z. Chowdhury, Ferroelectrics **494,** (2016) 19.

[21] A. M. M. Farea, S. Kumar, K. Mujasam Batoo, A. Yousef, Physica B Condens. Matter **403,** (2008) 684.

[22] J. C. Maxwell, Maxwell Treatise Preface, (1873).

[23] M. B. Hossen, A. K. M. A. Hossain, J. Magn. Magn. Mater. **387,** (2015) 24.

[24] C. G. Koop, Phys. Rev. **83,** (1951) 121.

[25] M. Arifuzzaman, M. B. Hossen, Results Phys. 16 (2020).

[26] M. M. Hossen, M. B. Hossen, J. Mater. Sci.: Mater. Electro **30,** (2019) 20801.

[27] M. Belal Hossen, A.K.M. Akther Hossain, J. Adv. Ceram. **4,** (2015) 217.

[28] P. K. Roy, J. Bera, J. Magn. Magn. Mater. **298,** (2006) 38.

[29] M. A. Gabal, J. Magn. Magn. Mater. **321**, (2009) 3144.

[30] Y. K. Dasan, B. H. Guan, M. H. Zahari, L. K. Chuan, PLoS One **12,** (2017) 0170075.

[31] P. K. Roy, J. Bera, Mater. Chem. Phys. **132,** (2012) 354.

[32] Z. Yue, J. Zhou, L. Li, H. Zhang, Z. Gui, J. Magn. Magn. Mater. **208,** (2000) 55.

[33] M. M. Costa, G. F. M. Pires Júnior, A. S. B. Sombra, Mater. Chem. Phys. **123,** (2010) 35.

[34] C. C. Hwang, J.S. Tsai, T.H. Huang, Mater. Chem. Phys. **93,** (2005) 330.

[35] N. Das, D. Bhattacharya, A. Sen, H.S. Maiti, Ceram. Int. **35,** (2009) 21.

[36] R. Valenzuela, Phys. Res. Int. **2012,** (2012) 2090.

[37] R. Valenzuela, T. Gaudisson, S. Ammar, J. Magn. Magn. Mater. **400,** (2016) 311.

[38] J. Z. Msomi, T. Moyo, T. B. Doyle, J. Magn. Magn. Mater. **310,** (2007) 2534.

[39] O. F. Caltun, L. Spinu, A. Stancu, L. D. Thung, W. Zhou, J. Magn. Magn. Mater. **242,** (2002) 160.

[40] W. C. Hsu, S. C. Chen, P. C. Kuo, C. T. Lie, W. S. Tsai, Mater. Sci. Eng. B **111,** (2004) 142

[41] I. Z. Rahman, T. T. Ahmed, J. Magn. Magn. Mater. **290,** (2005) 1576.

[42] S. Joshi, M. Kumar, H. Pandey, M. Singh, P. Pal, J. Alloys. Compd. **768,** (2018) 287.

[43] S. U. Haque, K. K. Saikia, G. Murugesan, S. Kalainathan, J. Alloys Compd. **701,** (2017) 612.

[44] Z. Yue, J. Zhou, L. Li, H. Zhang, Z. Gui, J. Magn. Magn. Mater. **208,** (2000) 55.

[45] A. K. M. A. Hossain, T. S. Biswas, T. Yanagida, H. Tanaka, H. Tabata, T. Kawai, Mater Chem. Phys. **120,** (2010) 461.

[46] X. Qi, J. Zhou, Z. Yue, Z. Gui, L. Li, J. Magn. Magn. Mater. **251,** (2002) 316.

[47] H. Moradmard, S. Farjami Shayesteh, P. Tohidi, Z. Abbas, M. Khaleghi, J. Alloys. Compd. **650,** (2015) 116.

[48] R. M. Rosnan, Z. Othaman, R. Hussin, A. A. Ati, A. Samavati, S. Dabagh, S. Zare, Chin. Phys. B **25,** (2016).

[49] B. Thangjam, I. Soibam, Int. J. Appl. Eng. **12,** (2017) 13201

[50] P. Chavan, L.R. Naik, P.B. Belavi, G. Chavan, C.K. Ramesha, R.K. Kotnala, J. Electron Mater. **46,** (2017) 188.

[51] S. m. kabbur, J. Electron Mater. **46,** (2017) 5693.

[52] V. K. Mittal, P. Chandramohan, S. Bera, M. P. Srinivasan, S. Velmurugan, S. V. Narasimhan. Solid State Commun. **137,** (2006) 6.

[53] C. V. Stan, C. M. Beavers, M. Kunz, N. Tamura, Quantum Beam Sci. **2** (2018).

[54] J. B. Nelson, D. P. Riley. Proc. Phys. Soc. **57,** (1945) 160.

[55] W. S. Sarifuddin, Utari, B. Purnama, AIP Conf. Proc. **2202**, (2019).

[56] A. Bagum, M. B. Hossen, F. U. Z. Chowdhury. Ferroelectrics **494,** (2016) 19.

[57] M. Naeem, N. A. Shah, I. H. Gul, A. Maqsood, J. Alloys Compd. **487** (2009) 739.

[58] K. O. Low, F. R. Sale. J. Magn. Magn. Mater. **246,** (2002) 30.

[59] J. F. Janak. J. Appl. Phys. **34,** (1963) 1119.

[60] D. Park, Phys. Rev. **98,** (1955) 438.

[61] U. Assistance. Lambda 365 PerkinElmer. 2016.

[62] G. Wita, Lambda X65 series UV/Vis Simplified for your Lab. 2015.

[63] J. Tauc, R. Grigorovici, A. Vancu, Physica Status Solidi. **15,** (1966) 627.

[64] E. A Davis, N.F. Mott. Philos. Mag. (Abingdon) **22,** (1970) 903.

[65] B. D. Viezbicke, S. Patel, B. E. Davis, D. P. Birnie, Phys. Status Solidi B Basic Res. **252,** (2015) 1700.

[66] R. Kumar, M. Kar, Ceram. Int. **42,** (2016) 6640.

[67] T. M. Hammad, S. Kuhn, A. A. Amsha, N. K. Hejazy, R. Hempelmann, Comprehensive J. Supercond. Nov. Magn. **33,** (2020) 3065.

[68] M. S. Sader, E. L. Moreira, V. C. A. Moraes, J. C. Araújo, R. Z. Legeros, G. A. Soares, Key Eng. Mater. **396,** (2009) 277.

[69] F. F. Alharbi, S. Aman, N. Ahmad, S. R. Ejaz, R. Y. Khosa, S. Abbas, A. G. Abid, M. S. Al-Buriahi, Z. A. Alrowaili, M. S. Waheed, J. Mater. Sci.: Mater. Electron. **33,** (2022) 12147.

[70] N. M. Deraz, A. Alarifi, J. Anal. Appl. Pyrolysis **94,** (2012) 41.

[71] N. Rezlescu, E. Rezlescu, C. Pasnicu, M.L. Craus, J. Phys.: Condens. Matter. **6,** (1994) 5707.

[72] K. Shankland, Refinement, J. Res. Natl. Inst. Stand. Technol. **109,** (2004) 143.

[73] L. Kumar, P. Kumar, A. Narayan, M. Kar, Int. Nano Lett. **3,** (2013).

[74] W. Dollase, Phys. Chern. Minerals **20,** (1994) 541

[75] M. F. Mahmood, M. B. Hossen, J. Mater. Sci.: Mater. Electron. **32,** (2021) 14248.

[76] R. Saravanan, K. S. S. Ali, S. Israel, J. Phys. Chem. Solids. **64,** (2003) 51.

[77] G. M. Santos, I. B. Catellani, R. D. Bini, G. H. Perin, L. F. Cótica, J. E. Padilha, V. F. Freitas, I. A. Santos, R. Guo, A. S. Bhalla, Ferroelectrics **500,** (2016) 26.

[78] R. Saravanan, Y. Ono, M. Isshiki, K. Ohno, T. Kajitani, J. Phys. Chem. Solids. **64,** (2003) 51.

[79] K. Somasundaram, K. P. Abhilash, V. Sudarsan, P. Christopher Selvin, R. M. Kadam, Physica B Condens. Matter. **491,** (2016) 79.

[80] S. Sarkar, R. Das, IJPAP **56,** (2018) 765.

[81] H. S. Im, K. Park, J. Kim, D. Kim, J. Lee, J. A. Lee, J. Park, J. P. Ahn, ACS Omega **3,** (2018) 3129

[82] D. N. Bhosale, S. R. Sawant, S. A. Gangal, R. R. Mahajan, P. P. Bakare, MSEB. **65,** (1999) 79.

[83] M. B. Hossen, A. K. M. A. Hossain, J. Magn. Magn. Mater. **387,** (2015) 24.

[84] S. S. Yattinahalli, S. B. Kapatkar, S. N. Mathad, Adv. Sci. Focus **2,** (2014) 42.

[85] M. I. Mendelson, J. Am. Ceram. **52,** (1969) 443

[86] M. Chaitanya Varma, S. Bharadwaj, G. S. V. R. K. Choudary, K. S. R. Murthy, K. H. Rao, Int. J. Mod. Phys. B **31,** (2017).

[87] B. J. Kellett, F. F. Lange, Thermodynamics of Densification: I, J. Am. Ceram. **72,** (1989) 725.

[88] M. P. Reddy, W. Madhuri, M. V. Ramana, N. R. Reddy, K. V. S. Kumar, V. R. K. Murthy, K. S. Kumar, R. R. Reddy, J. Magn. Magn. Mater. **322,** (2010) 2819.

[89] R. S. Devan, Y. D. Kolekar, B. K. Chougule, J. Condens. Matter. Phys. **18,** (2006) 9809.

[90] S. M. Patange, S. E. Shirsath, B.G. Toksha, S. S. Jadhav, K. M. Jadhav, J. Appl. Phys. **106,** (2009).

[91] M. B. Sahana, C. Sudakar, A. Dixit, J. S. Thakur, R. Naik, V. M. Naik, Acta. Mater. **60,** (2012) 1072.

[92] M. M. Eltabey, A. M. Massoud, C. Radu, J Nanomater. **2014,** (2014).

[93] D. Ahmad, N. Mehboob, A. Zaman, N. Ahmed, K. Ahmed, M. Mushtaq, K. Althubeiti, A. Ali, F. Sultana, K. Bashir, Coatings **11,** (2021).

[94] U. R. Ghodake, N. D. Chaudhari, R. C. Kambale, J. Y. Patil, S. S. Suryavanshi, J. Magn. Magn. Mater. **407,** (2016) 60.

[95] P. B. Belavi, G. N. Chavan, B. K. Bammannavar, L. R. Naik, R. K. Kotnala, AIP Conf. Proc. (2011) 1249

[96] D. Parajuli, N. Murali, A. V. Rao, A. Ramakrishna, Y. M. S, K. Samatha, S. Afr. J. Chem. Eng. **42,** (2022) 106.

[97] K. Raju, G. Venkataiah, D.H. Yoon, Ceram. Int. **40,** (2014) 9337.

[98] E. C. Devi, I. Soibam, J. Supercond. Nov. Magn. **32,** (2019) 1293.

[99] J. Massoudi, M. Smari, K. Nouri, E. Dhahri, K. Khirouni, S. Bertaina, L. Bessais, E.K. Hlil, RSC Adv. **10,** (2020) 34556.

[100] N. Amri, J. Massoudi, K. Nouri, M. Triki, E. Dhahri, L. Bessais, RSC Adv. **11,** (2021) 13256.

[101] Y. S. Koshkid'ko, E. T. Dilmieva, A. P. Kamantsev, A. V. Mashirov, J. Cwik, N. B. Kol'chugina, V. V. Koledov, V. G. Shavrov, J. Commun. Technol. Electron. **68,** (2023) 379.

[102] B. Rabi, A. Essoumhi, M. Sajieddine, E.K. Hlil, A. Razouk, & R. Moubah, & H. Lassri, J. Supercond. Nov. Magn. **33,** (2020) 2527.

[103] A. Anand, M. M, V. R. K, V. V. S, Y. S. Koshkid'ko, S. S, J. Magn. Magn .Mater. **528,** (2021).

[104] M. S. Anwar, F. Ahmed, G. W. Kim, S. N. Heo, B. H. Koo, JKPS **62,** (2013) 1974.

[105] I. Hussain, M.S. Anwar, E. Kim, B.H. Koo, C.G. Lee, Korean J. Mater. Res. **26,** (2016) 623.

[106] L. M. Thorat, J. Y. Patil, D. Y. Nadargi, U. R. Ghodake, R. C. Kambale, and S. S. Suryavanshi, J. Solgel Sci. Technol **86**, (2018) 731.

[107] R. S. Devan, Y. D. Kolekar, and B. K. Chougule, J. Condens. Matter Phys. **18**, (2006) 9809.

[108] S. M. Patange, S. E. Shirsath, B. G. Toksha, S. S. Jadhav, and K. M. Jadhav, J Appl. Phys. **106**, (2009).

[109] J.C. MAXWELL, Maxwell Treatise Preface, (1873).

[110] D. Varshney, A. Kumar, and K. Verma, J. Alloys. Compd. **509**, (2011) 8421.

[111] N. Singh, A. Agarwal, S. Sanghi, and P. Singh, Physica B Condens. Matter **406**, (2011) 687.

[112] A. K. Singh, T. C. Goel, R. G. Mendiratta, O. P. Thakur, and C. Prakash, J. Appl. Phys. **91**, (2002) 6626.

[113] N. Sivakumar, A. Narayanasamy, N. Ponpandian, and G. Govindaraj, J Appl Phys **101**, (2007).

[114] Z. Ahmad, S. Atiq, S. K. Abbas, S. M. Ramay, S. Riaz, and S. Naseem, Ceram Int **42**, (2016) 18271.

[115] E. H. Rhoderick, J. Phys. D: Appl. Phys. **3,** (1970) 1153.

[116] S. F. Chérif, A. Chérif, W. Dridi, and M. F. Zid, Arab. J. Chem **13**, (2020) 5627.

[117] R. Rathika, O. Padmaraj, and S. A. Suthanthiraraj, Ionics (Kiel) **24**, (2018) 243.

[118] R. M. Hill and L. A. Dissado, J. Phys. C: Solid State Phys. **18,** (1985) 3829.

[119] S. M. Khan, M. Sharmin, M. N. I. Khan, A. K. M. Akther Hossain, and M. D. Rahaman, J. Mater. Sci. Mater. Electron. **30**, (2019) 15388.

[120] T. Prakash, K. P. Prasad, R. Kavitha, S. Ramasamy, B. S. Murty, J Appl Phys **102**, (2007).

[121] R. S. Yadav, I. Kuřitka, J. Vilcakova, J. Havlica, L. Kalina, P. Urbánek, M. Machovsky, D. Skoda, and M. Masař, J. Mater. Sci.: Mater. Electron. **29**, (2018) 15878.

[122] B. J. Hunt, Phys. Today, **48,** (2012).

[123] T. Nakamura, J Magn Magn Mater **168,** 285(1997)

[124] C. Sujatha, K. V. Reddy, K. S. Babu, A. R. Reddy, K. H. Rao, Ceram Int **38**, (2012) 5813.

[125] K. H. Maria, U. S. Akther, I. N. Esha, M. S. Hossain, M. N. I. Khan, J Supercond Nov Magn **33**, (2020) 2133.